Chapter 1
Liquid Carbon: Freezing Line and Structure Near Freezing

Luca M. Ghiringhelli[1] and Evert Jan Meijer[2]

Abstract This chapter deals with the phase diagram of carbon with emphasis on the liquid phase occurring in extreme conditions of temperature and pressure. After presenting a critical review of the experimental results and still unresolved issues, the authors discuss the possibility of modeling carbon by use of empirical potentials. Also the techniques to evaluate numerically the free energy of each phase are presented in detail. The second part of the chapter discusses in detail the structure of the liquid in different ranges of pressure, the pressure–density equations of state at different temperatures and the possibility of a liquid–liquid phase transition.

1.1 Introduction

Carbon exhibits a rich variety of solid structures such as the familiar crystalline graphite and diamond state, or amorphous states such as glassy carbon or carbon black. More recently additional (metastable) phases have been found or predicted. These include carbynes [1, 2] and M-carbon [3]. In addition to the bulk phases there are various other recently discovered structures including fullerenes [4], nanotubes [5], and graphene [6].

Knowledge of the phase diagram of carbon is of crucial importance for a better understanding of a wide variety of physical phenomena and properties of carbon-based materials. For example, the phase diagram determines the carbon content of the interior of the Earth and other planets and it determines the optimal conditions for the manufacturing of synthetic diamonds. Knowledge of the graphite melting line is relevant for the formation mechanism of low dimensional layered structures that are important in fundamental and technological applications.

[1]Fritz Haber Institute of the Max Planck Society, Faradayweg 4-6, D-14195, Berlin, Germany
e-mail: luca@fhi-berlin.mpg.de

[2]Van't Hoff Institute for Molecular Sciences & Amsterdam Center for Multiscale Modeling, Universiteit van Amsterdam, Nieuwe Achtergracht 166, NL-1018 WV, Amsterdam, The Netherlands
e-mail: e.j.meijer@uva.nl

L. Colombo and A. Fasolino (eds.), *Computer-Based Modeling of Novel Carbon Systems and Their Properties*, Carbon Materials: Chemistry and Physics 3,
DOI 10.1007/978-1-4020-9718-8_1,

The phase diagram of carbon has been intensively studied, both experimentally and by theoretical and numerical methods [1, 7–11, 11–26]. These studies covered pressures (P) and temperatures (T) ranging up to 100 GPa and 10,000 K. Until recently the knowledge of the carbon phase diagram was still fragmented because experiments under these conditions are difficult if not outright impossible, whereas quantitative theoretical and numerical predictions were hampered by the fact that the existing atomistic models for carbon had serious flaws that made them unsuited for quantitative predictions. Recent advances in modeling of carbon allows for the calculation of the phase diagram of carbon and the structure of the liquid with unprecedented accuracy. This provided significant progress in the understanding of the behavior of carbon under extreme conditions [26–30]. Knowledge of the location of the melting line and the liquid structure near melting is an important requisite in understanding the (non)-existence of a liquid–liquid phase transition and the process of homogeneous nucleation of the liquid into graphite or diamond. The latter issue is key to answering the question of the existence of diamond in planet interiors.

In the present contribution we provide a review of some of the recent computational studies of the phase diagram and the liquid structure of carbon. First, we summarize some important characteristics of the carbon phase diagram. Then we discuss the modeling of the inter-atomic interaction with a focus on a particular class of bond-order potentials, the so-called LCBOP models. Subsequently we discuss in detail the computational methods to determine the thermodynamic stability of the diamond, graphite, and liquid phase together with a presentation of the calculated phase diagram for a well tested version of the LCBOP model. These results are discussed in a context of experimental and other computational studies. Finally, we address the structure of liquid carbon.

1.2 Carbon Phase Diagram: Some Important Characteristics

In the pressure and temperature range up to 100 GPa and 10,000 K, the well established thermodynamic stable phases of carbon are the crystalline graphite (G) and diamond (D) phase at lower temperatures, and a liquid (L) phase at higher temperatures (Fig. 1.4). The graphite-diamond coexistence line has been relatively well characterized up to 2,400 K [7, 15]. For the graphite melting line a large amount of experimental data are available [1, 8, 9, 13, 14, 16]. The experiments have in common that the melting temperature shows little variation with pressure, and that most of the measured graphite melting $P - T$ lines [8, 9, 16] show a maximum around $P = 6$ GPa. However, the nature of the maximum is not well established. The experimental estimates for the melting temperatures show a large spread. It appears that the estimated melting temperature depends significantly on the heating rate of the sample [13, 14], yielding values from 3,700 to 5,000 K below 0.01 GPa. In a recent comprehensive review of graphite melting [31] the melting temperature is proposed to be in the range of 4,600–5,000 K. The precise nature of the maximum in the melting curve is important, because a discontinuous change of slope of the melting curve

at this point would imply the existence of a liquid–liquid phase transition (LLPT) line, branching off from the graphite melting curve. This will be discussed in more detail in Section 1.5.

Early shock wave experiments [11] provided evidence for the existence of diamond at $P = 140$ GPa at a temperature beyond the temperature of the Graphite–Diamond–Liquid triple point (T $\sim$ 4,000 K), implying that the carbon diamond melting line has a positive slope in the $P - T$ diagram. Recent experimental data have provided evidence [32] that diamond is stable up to at least 800 GPa.

1.3 Modeling Carbon

Realistic modeling of the carbon phase diagram involving the liquid, graphite, and diamond phase requires an accurate description of the inter-atomic interactions, combined with a precise evaluation of the relative stability of the involved phases. This requires the evaluation of the free energy of state points in all phases involved. Presently, density-functional theory (DFT) based ab initio MD simulations would provide the best possible approach. However, the computational cost associated with DFT calculations renders such an approach unfeasible, in particular when combined with free-energy calculations.

A viable alternative is to model the inter-atomic interactions by a functional description, whose parameters are (partly) fitted to a selected database. Such a functional description (also referred to as empirical, semi-empirical or classical potentials) serves several purposes, ranging from the modeling of minimum energy structures for surface reconstructions, grain boundaries or related defects, to the description of the liquid structure and thermodynamic stability.

According to Brenner [33], an analytic potential needs to be:

- *Flexible* The function should be flexible enough to accommodate the inclusion of a relatively wide range of structures in a fitting database.
- *Accurate* The potential function must be able to accurately reproduce quantities such energies, bond lengths, elastic constant, and related properties entering a fitting database.
- *Transferable* The functional form of the potential should be able to reproduce related properties that are *not* included in the fitting database. In practice the potential should be able to give a good description of the energy landscape for any possible realistic configuration characterized by the set of atomic positions $\{\mathbf{r}_i\}$.
- *Computationally Efficient* The function should be of such a form that it is tractable for a desired calculation, given the available computing resources.

Focusing on carbon, there is a noble lineage of increasingly successful parameterizations of the empirical potentials, from the Tersoff [34] potential, via the Brenner potentials [35] and their modifications [36–39] up to Los-Fasolino LCBOP [27,29]. The crucial characteristic of these potentials is that they account for the "bond order" : the potentials formalize and parameterize the idea that for covalently bonded

systems an increasing number of bonds per atom modifies (typically decreases) the bond energy *per bond*. With increasing complexity, many-body contributions due to angular correlations [34], conjugation effects [35] and torsional interactions [36] were included. These short ranged potentials proved to describe increasingly well hydrocarbon molecules (when hydrogen is included) and the diamond phase. However, more disordered structures were less well described. After an earlier attempt to introduce longer range (pair) correlations [38], the seamless inclusion of non-bonded interactions led to the semi-empirical long range bond order potential (LCBOPI) by Los and Fasolino [27] that is partly based on ab initio data. The inclusion of conjugation dependent torsional interactions (LCBOPI$^+$) (Ref. [29] in Appendix A, and Ref. [40] in chapter 6.7) added the necessary flexibility to describe in a proper way the transformation between diamond and graphite and the structure of the liquid phase. LCBOPI$^+$ also accounts properly for the inter-planar interactions in graphite. In a subsequent development, the introduction of middle range interactions (i.e. allowing for smooth bond breaking and forming), together with a revision of the definition of the torsional angle, yielded LCBOPII [29], which performs as well as density functional in the liquid phase (wherever it was tested) and opens the way for an accurate description of surfaces and their reconstructions.

The LCBOP family is the first empirical potential that is capable of providing an accurate description of the graphite, diamond, and liquid phase. This makes the LCBOP's uniquely suited to predict the carbon phase diagram and the properties of liquid carbon.

1.4 The Graphite–Diamond–Liquid Phase Diagram of LCBOPI$^+$

1.4.1 Computational Methods

The properties of the liquid, graphite, and diamond phases were determined by Monte Carlo (MC) simulations. Coexistence lines were determined by locating points in the $P - T$ diagram with equal chemical potential for the two phases involved. To this purpose, we first determined the chemical potential for the liquid, graphite, and diamond at an initial state point ($P = 10$ GPa, $T = 4{,}000$ K). Subsequently, the liquid/graphite, liquid/diamond, and graphite/diamond coexistence pressures at $T = 4{,}000$ K were located. In turn, these coexistence points served as the starting point for the determination of the graphite melting, diamond melting, and graphite/diamond coexistence lines, obtained integrating the Clausius–Clapeyron equation (this procedure is also known as Gibbs–Duhem integration):

$$\frac{\mathrm{d}T}{\mathrm{d}P} = \frac{T\Delta v}{\Delta h} \tag{1.1}$$

where Δv is the difference in specific volume, and Δh the difference in molar enthalpy between the two phases (calculated as $h = u + Pv$, being u the potential energy per particle).

The first point is in turn accomplished in two sub-steps. Firstly a Helmholtz free energy (F) at a given volume (V) and temperature (T) can be calculated via thermodynamic integration. In a canonical system, coexistence between phases can be found via the Helmholtz double tangent construction, after F is evaluated at other V and T, by integrating its gradient, a quantity that can be measured in a MC simulation (see e.g. Ref. [21]). As an alternative [41], the one we chose, one can transform F into the chemical potential μ (coinciding with the specific Gibbs free energy in a one-component system), the latter as a function of P and T, knowing accurately enough the equation of state of each phase. Coexistence at a given T is found at that P where μ for the different phases cross.

For all phases, the free energies at the initial state point F^{Φ} was determined by transforming the systems into a reference system F^{ref} of known free energy, using $U_\lambda = (1-\lambda)U^{\Phi} + \lambda U^{\mathrm{ref}}$. Here, U^{Φ} and U^{ref} denote the potential energy function of the LCBOPI$^+$ and of the reference system, respectively. The transformation is controlled by varying the parameter λ continuously from 0 to 1. The free-energy change upon the transformation was determined by thermodynamic integration:

$$\begin{aligned} F^{\Phi} &= F^{\mathrm{ref}} + \Delta F^{\mathrm{ref}\to\Phi} \\ &= F^{\mathrm{ref}} + \int_{\lambda=0}^{\lambda=1} d\lambda \left\langle \frac{\partial U_\lambda}{\partial \lambda} \right\rangle_\lambda \\ &= F^{\mathrm{ref}} + \int_0^1 \mathrm{d}\lambda \left\langle U^{\mathrm{ref}} - U^{\Phi} \right\rangle_\lambda \end{aligned} \tag{1.2}$$

The symbol $\langle ... \rangle_\lambda$ denotes the ensemble average with the potential U_λ.

For the liquid phase the reference system was taken to be a Lennard–Jones 12-6 (LJ) system, described by the well known interaction energy:

$$U^{LJ} = 4\varepsilon \left(\left(\frac{\sigma}{r}\right)^{12} - \left(\frac{\sigma}{r}\right)^{6} \right)$$

The reference free energy (F^{ref}) of the liquid is:

$$F^{\mathrm{ref}} = F^{\mathrm{LJ}} = F^{\mathrm{id}} + F^{\mathrm{ex}}_{\mathrm{LJ}} \tag{1.3}$$

The ideal-gas contribution is:

$$\frac{\beta F^{\mathrm{id}}}{N} = 3\ln\Lambda + \ln\rho - 1$$

where N is the number of particles in the box, $\Lambda = h/\sqrt{2\pi m k_B T}$ is the de Broglie wavelength, m is the mass of one atom, and ρ is the number density. The LJ liquid excess free energy ($F^{\mathrm{ex}}_{\mathrm{LJ}}$) has been accurately parameterized [42] by means of (NVT) MC and MD simulations.

The LJ σ parameter was determined by matching the first peak of the radial distribution functions ($g(r)$) of the LCBOPI$^+$ and LJ liquid at the same position, ensuring optimal similarity between the structure of the two liquids. The LJ ε parameter was chosen such that, at the selected $T = 4{,}000\,\mathrm{K}$, the LJ liquid was above the critical temperature: this is done in order to avoid possible unwanted transitions, since the thermodynamic integration method works under the hypothesis that no boundary between phases is ever crossed on varying λ. On the other hand, the liquid should not be too far from the critical temperature: in fact, the $g(r)$ given by the LCBOPI$^+$ (see Section 1.5) has pronounced secondary peaks beyond the first coordination shell. Thus, a rather structured LJ liquid had to be preferred for the coupling. The requirements are matched by putting the LJ liquid in proximity of the critical temperature.

For the solid phases the Einstein crystal, whose free energy is analytically known, was taken as reference system [43]. For the Einstein solid, U^E is:

$$U^E = \frac{\alpha}{2} \sum_{i=1}^{N} (\mathbf{r}_i - \mathbf{r}_{i,0})^2$$

where the $\mathbf{r}_{i,0}$ are the equilibrium (i.e. at $T = 0\,\mathrm{K}$) lattice positions of the particles. In the Einstein solid, the fixed equilibrium lattice positions are referred to an absolute frame, so that if a particle is moved, then the crystal as a whole cannot. When $\lambda \sim 0$ (i.e. the system is on the LCBOPI$^+$ side) the center of mass of the system (CoM) is free to drift: if L is the box size, the CoM mean square displacement $\langle r^2 \rangle_{CoM}$ becomes of the order of L^2. Should this happen, the integral of Eq. 1.2 becomes sharply peaked for small values of λ. In fact, the particles are allowed to drift far away from their absolute equilibrium lattice positions, since the coupling with the Einstein solid is mild, but in Eq. 1.2 appears the energy $U^{\Phi} = U^E$, that can become uncontrollably large. In order to circumvent this problem for small λ, a physically well founded remedy is to perform a simulation under the constraint that the CoM of the solid is fixed [43–45], so that $\langle r^2 \rangle_{CoM}$ is of the order of $\langle r^2 \rangle_0$, the mean square displacement of a particle from its lattice site in a real (i.e. interacting) crystal. This constraint calls for a slight modification of Eq. 1.2. We label with $E(CM)$ the Einstein solid with fixed center of mass, $\Phi(CM)$ the LCBOPI$^+$ system with fixed center of mass, so that [43–45]:

$$\begin{aligned} F^{\Phi} &= F^{\mathrm{E(CM)}} + \Delta F^{\mathrm{E(CM)} \to \Phi(CM)} + \Delta F^{\Phi(\mathrm{CM}) \to \Phi} \\ &= F^{\mathrm{E(CM)}} + \int_0^1 \mathrm{d}\lambda \left\langle U^{\mathrm{ref}} - U^{\Phi} \right\rangle_{\lambda} + \Delta F^{\Phi(\mathrm{CM}) \to \Phi} \end{aligned} \tag{1.4}$$

Specifically:

$$\frac{\beta F^{\mathrm{E(CM)}}}{N} = 3 \ln \Lambda - \frac{3}{2} \ln \left(\frac{2\pi}{\beta \alpha} \right) - \frac{3}{2N} \left(\ln \left(\frac{\alpha \beta}{2\pi} \right) + \ln N \right) \tag{1.5}$$

The last term on the right hand side represents the (finite size) correction for the fixing of the CoM. Note its dependency on $1/N$, which consistently makes the correction vanish in the thermodynamic limit.

$$\frac{\beta\Delta F^{\Phi(\mathrm{CM})\to\Phi}}{N} = -\frac{1}{N}\ln\frac{V}{N_{ws}} \tag{1.6}$$

where N_{ws} is the number of Wigner–Seitz cells in the simulation box. If n_{ws} is the number of atoms per Wigner–Seitz cell, $N_{ws} = N/n_{ws}$. Note that also this term, a purely finite size effect, vanishes in the thermodynamic limit.

In reporting the results (in Section 1.4.2) we will group differently the terms of the previous three equations: it is indeed natural to group the terms proportional to $\frac{1}{N}$, so that:

$$\frac{\beta F^{\mathrm{E}}}{N} = 3\ln\Lambda - \frac{3}{2}\ln\left(\frac{2\pi}{\beta\alpha}\right) \tag{1.7}$$

$$\frac{\beta\Delta F^{\frac{1}{N}}}{N} = -\frac{1}{N}\left(\frac{3}{2}\ln\left(N\,\frac{\alpha\beta}{2\pi}\right) + \ln\frac{V}{N_{ws}}\right) \tag{1.8}$$

The coupling of (hot) graphite to an Einstein crystal, whose average atomic positions are constrained to a fixed reference system, displayed a peculiar feature. Due to the softness of the interplanar interactions (0.07 $\mathrm{k_B T}$ at 4,000 K), graphite neighboring sheets are allowed to slide. Also this is a finite size effect: to correct for this we found necessary to attach any sheet to its CoM, independently from the others.[1]

The Einstein crystal spring constant, α, was determined by requiring that the mean-squared displacement from the equilibrium lattice positions is equal for the Einstein crystal and the carbon crystal:

$$\frac{3}{\beta\alpha} = \left\langle \frac{1}{N}\sum_{i=1}^{N}(\mathbf{r}_i - \mathbf{r}_{i,0})^2 \right\rangle$$

Therefore α was fixed by calculating the right hand side in a simulation with the LCBOPI$^+$.

[1] Equation 1.5 then becomes:

$$\frac{\beta F^{\mathrm{E(CM)}}}{N} = 3\ln\Lambda - \frac{3}{2}\ln\left(\frac{2\pi}{\beta\alpha}\right) - \frac{3N_s}{2N}\left(\ln\left(\frac{\alpha\beta}{2\pi}\right) + \ln N N_s\right)$$

where N_s is the number of sheets. Equation 1.6 becomes:

$$\frac{\beta\Delta F^{\Phi(\mathrm{CM})\to\Phi}}{N} = -\frac{N_s}{N}\ln\frac{V}{N_{ws}}$$

where, in $N_{ws} = N/n_{ws}$, one has to define the Wigner–Seitz cell within a graphite sheet; this leads to $n_{ws} = 2$. Equation 1.8 becomes:

$$\frac{\beta\Delta F^{\frac{1}{N}}}{N} = -\frac{N_s}{N}\left[\frac{3}{2}\ln\left(N N_s\,\frac{\alpha\beta}{2\pi}\right) + \ln\frac{V}{N_{ws}}\right].$$

Table 1.1 Parameters for the polynomial fitting of the 4,000 K isotherms of the three phases, according to: $P(\rho) = a + b\rho + c\rho^2$

	a [GPa]	b [GPa nm^3]	c [GPa nm^6]
Liquid	89.972	−1.9654	0.011 092
Diamond	74.809	−3.6307	0.019 102
Graphite	108.29	−2.2707	0.011 925

In order to estimate the chemical potential μ along the 4,000 K isotherm we integrated from the initial state point a fit, $P(\rho) = a + b\rho + c\rho^2$, through simulated (P, T) state points along the 4,000 K isotherm. Here, ρ is the number density, and a, b, and c are fit parameters (see Table 1.1). This yields for the chemical potential [41]:

$$\beta\mu(\rho) = \frac{\beta F^{\Rightarrow}}{N} + \beta\left[\frac{a}{\rho^{\Rightarrow}} + b\,\ln\frac{\rho}{\rho^{\Rightarrow}} + b + c\left(2\rho - \rho^{\Rightarrow}\right)\right] \tag{1.9}$$

Here, $\rho^{\Rightarrow}$ denotes the number density at the initial state point, N the number of particles, and $\beta = 1/k_{\mathrm{B}}T$, with k_{B} the Boltzmann constant. Details on this equation are given in Appendix A.

1.4.2 The LCBOPI$^+$ Phase Diagram

For calculating the three $F^{\Rightarrow}$ we performed independent Monte Carlo (MC) simulations for three phases. Three samples of 216 particle of the three systems were prepared, the solids in their lattice positions, and the liquid in a simple cubic arrangement. The three phases were equilibrated with NPT MC simulations at the chosen $T = 4{,}000$ K and at $P = 10$ GPa.[2] The integer N = 216 permits the atoms to be arranged both in a defect-free diamond and cubic lattice, aligned with the sides of a cubic cell, while bonding perfectly across its faces to periodic-image atoms. The same requirements are fulfilled for 216 atoms in a defect-free graphite lattice, arranged in three sheets, but in a rectangular periodically replicated cell, with resulting edge-size ratios 1:1.5:1.7. The first, in-plane, ratio (1:1.5) is defined by the lattice geometry (hexagons), while the interplanar ratio (1:1.7) is pressure dependent. In fact, the rescaling of the box was allowed to be independent on the three axes for the equilibration of the solid phases, while kept intrinsically isotropic for the melting of the cubic crystal and the subsequent equilibration of the liquid phase. The equilibrium densities $\rho^{\Rightarrow}$, expressed in 10^3 kg/m^3, were 3.425 for diamond, 2.597 for graphite, and 2.421 for the liquid. Three configurations at the equilibrium volume were then chosen as starting points for the three thermodynamic integrations. The value of α

[2] For the correct application of the method it is not needed to have the three states at the same P. It is only required that the phases share a broad stable region in pressure at the chosen T.

was set to 453,000 and 39,700 kJ/(mol nm^2) for diamond and graphite, respectively. The parameters σ and ε for the LJ fluid were 0.127 nm and 31.84 kJ/mol.

The reference free energies $\beta F^{\mathrm{E}}/N$ were $-5.755\ k_BT$, and $-1.912\ k_BT$ for graphite and diamond, respectively, while the reference free energy for the liquid was found $(\beta/N)\left(F^{\mathrm{id}} + F^{\mathrm{ex}}_{\mathrm{LJ}}\right) = -10.863\ k_BT$. The integration in Eq. 1.2 yields for $\beta F^{\Phi}/N$ the values $-25.090 \pm 0.006\ k_BT$ (graphite), and $-24.583 \pm 0.002\ k_BT$ (diamond), $-25.137 \pm 0.002\ k_BT$ (liquid).

The values of λ for the sampling were defined by a 10-point Gauss–Legendre integration scheme. The scheme avoids the sampling of the systems at the two boundary values of λ. A 10 point scheme assures exact result whenever the integrand function of Eq. 1.2 $\left(\langle U^{\mathrm{ref}} - U^{\mathrm{LCBOPI}^+}\rangle_\lambda\right)$ can be reasonably described with a polynomial up to order $2 * 10 + 1 = 21$. When $\lambda = 0, 1$ the system performs its random walk on the basis of only one of the two potentials, thus in principle is allowed to assume configurations completely avoided by the other potential, in such a way that the integrand of Eq. 1.2 could diverge. Should this be the case, the integration scheme would yield a poor estimate of the integral. We thus ascertained that the integrand never indeed diverged at $\lambda = 0, 1$. For the three phases, we run at each λ point an NVT MC simulation of 500,000 cycles.

In Fig. 1.1 $\langle U^{\mathrm{ref}} - U^{\mathrm{LCBOPI}^+}\rangle_\lambda$ versus λ is shown. The absence of spurious phase boundary crossings throughout the integration over λ was checked by looking at the

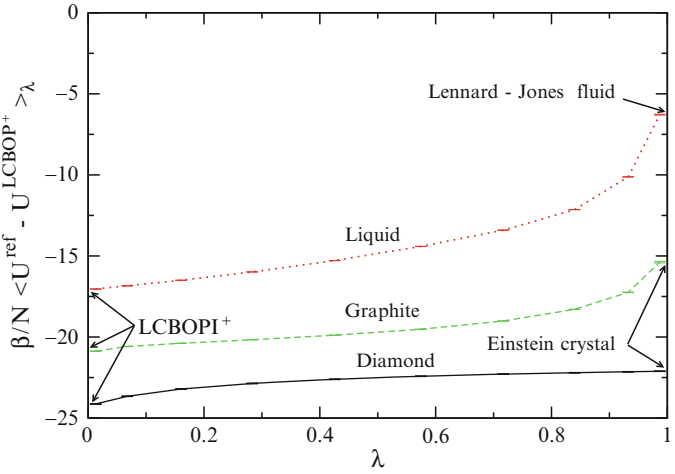

Fig. 1.1 Plots of the quantity $\beta/N\ \langle U^{\mathrm{ref}} - U^{\mathrm{LCBOPI}^+}\rangle_\lambda$ (see Eqs. 1.2 and 1.4) as a function of the coupling parameter λ for the liquid, graphite, and diamond phase. On the *left side* of the horizontal axis ($\lambda = 0$) is the pure LCBOPI$^+$. On the *right side* ($\lambda = 1$) is the reference system, i.e. the Lennard–Jones liquid for the liquid phase and two Einstein crystals (with different coupling constant) for graphite and diamond phase. The temperature is 4,000 K and the pressure is 10 GPa for the three phases, at $\lambda = 0$ (along the integration path the volume, rather than the pressure, is conserved). The simulated λ-points are marked by their *error bars*, that are almost reduced to a single dash at this scale

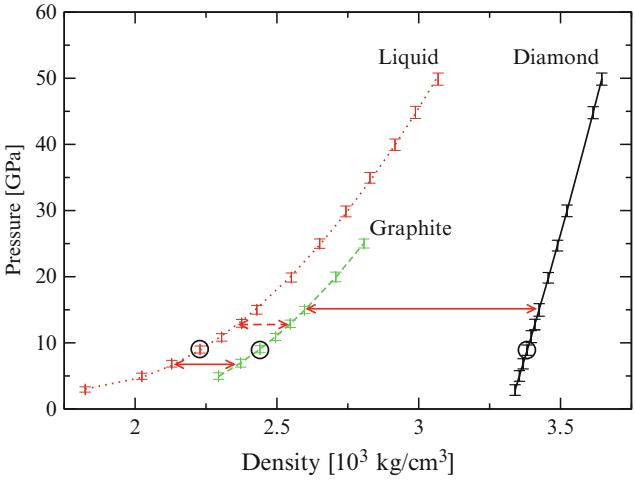

Fig. 1.2 Equations of state at 4,000 K for the liquid, graphite, and diamond phase. The *lines* are the quadratic polynomial fits to the data. The *circles* indicate the points, at 10 GPa, where the thermodynamic integration (Eq. 1.2) was performed. The *solid arrows* connect coexisting (stable) points, i.e. liquid/graphite and graphite/diamond. The *dashed arrow* links the liquid/diamond coexisting point, that is metastable relative to the graphite phase

distribution of $(U^{\text{ref}} - U^{\text{LCBOPI}^+})$.[3] Since the points were run in parallel in order to accumulate more statistics, only shorter independent simulations were performed by increasing and then decreasing λ, each new λ point starting from the final configuration of the previous. The absence of hysteresis in this process completely rules out phase boundary crossings. The isotherms for the three phases, calculated via NPT MC simulations together with their fit, are shown in Fig. 1.2.

The three μ curves (at $T = 4{,}000$ K), as given in Eq. 1.9, but expressed as functions of P, are shown in Fig. 1.3. The three curves, μ_{L}, μ_{G}, μ_{D}, as given in Eq. 1.9, intersect in pairs in three points (these points are shown as a solid triangle, square and diamond in Fig. 1.4). The intersections locate the graphite/liquid coexistence at 6.72 $\pm$ 0.60 GPa ($\mu_{\text{GL}} = -24.21 \pm 0.10\ k_{\text{B}}T$), and the graphite/diamond coexistence at 15.05 $\pm$ 0.30 GPa ($\mu_{\text{GD}} = -23.01 \pm 0.03\ k_{\text{B}}T$). The third intersection locates a diamond/liquid coexistence at $= 12.75 \pm 0.20$ GPa ($\mu_{\text{DL}} = -23.24 \pm 0.03\ k_{\text{B}}T$). Even though both diamond and the liquid are there metastable, this point can be taken as the starting one for the Clausius–Clapeyron integration of the diamond melting line. Starting from the three coexistence points at 4,000 K, the coexistence lines were traced–by integrating the Clausius–Clapeyron equation using the trapezoidal-rule predictor-corrector scheme [46]. The new value of the coexisting P at a given T was taken when two iterations differed less than 0.01 GPa, this being the size of the single uncertainty in the calculation of $\mathrm{d}P/\mathrm{d}T$. This normally took two to three iterations to be obtained.

[3] The distribution usually exhibits a bimodal shape in case of phase boundary crossing.

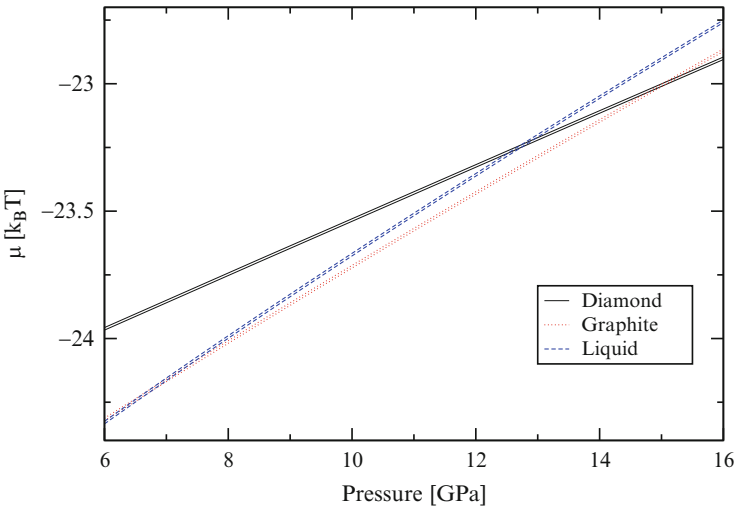

Fig. 1.3 Plot of the chemical potential μ for the three phases at $T = 4{,}000$ K; we plot *double lines*, which marks the boundaries of the numerical uncertainty of the calculated μ. These curves represent Eq. 1.9, but are expressed as a function of pressure using $P(\rho) = a + b\rho + c\rho^2$. The main source of error was the thermodynamic integration; the uncertainty in the equations of state was at least an order of magnitude less

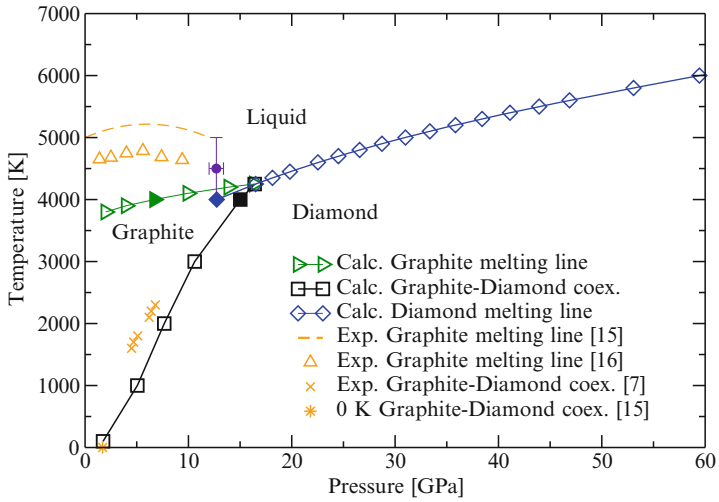

Fig. 1.4 Phase diagram of carbon up to 60 GPa. The *solid right triangle*, *square*, and *diamond* are the three coexistence points found by equating the chemical potentials at 4,000 K (see text). The *open right triangles*, *squares*, and *diamonds* are the calculated coexistence points, propagated via Gibbs–Duhem integration. The *solid circle* with *error bars* indicates the experimental estimate for the liquid/graphite/diamond triple point [15, 18, 20]. The *dashed line* is the experimental graphite *melting line* from Ref. [15]. The *up triangles* are graphite melting state points from Ref. [16]. The *crosses* represent experimental graphite/diamond coexistence from Ref. [7]. The *asterisk* represent the theoretical graphite/diamond coexistence at zero kelvin, as reported in Ref. [15]

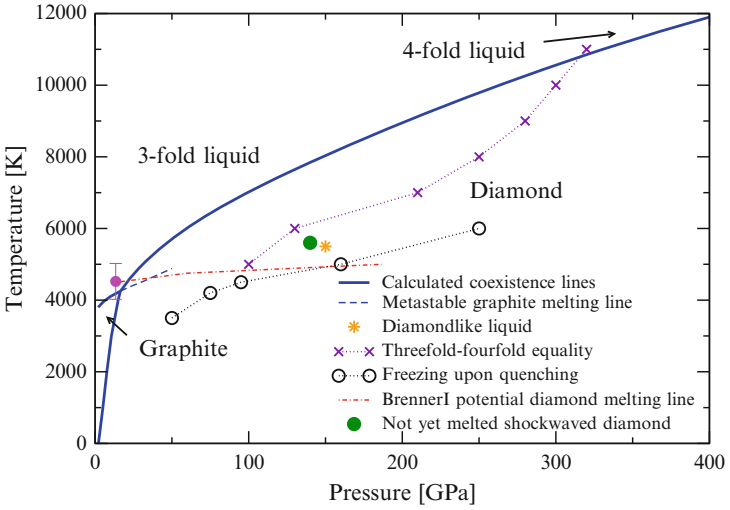

Fig. 1.5 Phase diagram of carbon at all calculated pressures. The thick *solid lines* are the calculated phase boundaries. The *dashed line* is the metastable prolongation of the graphite *melting line*, from Gibbs–Duhem integration; the line stops just before the simulated graphite became instable, displaying large density fluctuations. The *dashed-dotted line* departing from the experimental guess for the triple point (*solid circle* with *error bar* [15,18,20]) is the diamond *melting line* calculated in Ref. [21] with the BrennerI potential. The *solid circle* is the final point of the shock wave experiment of Ref. [11] at which diamond is not yet melted. Crosses mark the liquid with equal amount of three- and fourfold atoms; *circles* represent state points in which the sample freezes; in the region in between the two series is the "diamond-like liquid": the star is the point reported in Ref. [47]

Table 1.2 Pressure (P), temperature (T), solid and liquid densities (ρ) along the melting lines

P [GPa]	T [K]	ρ_G [10^3 kg/m^3]	ρ_L [10^3 kg/m^3]
Graphite melting line:			
2.00	3,800	2.134	1.759
6.70	4,000	2.354	2.098
16.4	4,250	2.623	2.414
Diamond melting line:			
16.4	4,250	3.427	2.414
25.5	4,750	3.470	2.607
43.9	5,500	3.558	2.870
59.4	6,000	3.629	3.043
99.4	7,000	3.783	3.264
148.1	8,000	3.960	3.485
263.2	10,000	4.286	3.868
408.1	12,000	4.593	4.236

The calculated phase diagram in the $P-T$ plane is shown in Fig. 1.4 for the low pressure region, and in Fig. 1.5 for the full range of pressures and temperatures considered. Table 1.2 lists the densities of selected points on the coexistence lines. The three coexistence lines meet in a triple point at 16.4 $\pm$ 0.7 GPa and 4,250 $\pm$ 10 K.

Table 1.3 Pressure (P), temperature (T), and melting enthalpy (Δh_m, calculated as the enthalpy of the liquid subtracted of the enthalpy of the underlying solid phase) along the melting lines

P [GPa]	T [K]	Δh_m [kJ/mol]
Graphite melting line:		
2.00	3,800	68.8
5.24	3,950	65.6
9.94	4,100	67.8
16.4	4,250	64.7
Diamond melting line:		
16.4	4,250	95.9
25.5	4,750	111.5
43.9	5,500	130.8
59.4	6,000	143.9
99.4	7,000	160.5
148.1	8,000	174.7
263.2	10,000	195.3
330.5	11,000	208.1
408.1	12,000	221.7

The graphite/diamond coexistence line agrees very well with the experimental data. In the region near the liquid/graphite/diamond triple point, that has not been directly probed in experiments, the graphite/diamond coexistence line bends to the right, departing from the usually assumed straight line. Analysis of our data shows this is mainly due to the fast reduction with increasing pressure of the interplanar distance in graphite at those premelting temperature. This causes an enhanced increase of the density in graphite, yielding a decrease of $\mathrm{d}T/\mathrm{d}P$.

Table 1.3 shows the melting enthalpy Δh_m for graphite and diamond. These are calculated as the difference in enthalpy between the solid and the melt at coexistence. Our calculated melting enthalpies of graphite are sensibly lower than the values around 110 kJ/mol reported in shock heating melting experiments in the past years [15, 16], nonetheless our values retain the feature of being rather constant along the graphite melting line. No experimental data are known about the melting enthalpies of diamond: we note that they increase monotonically with temperature (and pressure).

The calculated graphite melting line is monotonically increasing in a small temperature range around 4,000 K. In contrast to data inferred from experiments it shows no maximum and is at a somewhat lower temperature. In agreement with the experiments the coexistence temperature is only slowly varying with pressure. Inspection reveals that this behavior is due to (1) the limited variability of the melting enthalpy, and (2) a similar bulk modulus for liquid and graphite such that Δv is almost constant.

We have extended the calculation of the graphite melting line to the region in which both graphite and the liquid are metastable towards diamond, with the aim to look for a possible maximum in the line. The results are shown as a dashed line in Fig. 1.5. We stopped the Gibbs–Duhem integration at $\sim$50 GPa, where the 216-particles graphite sample started showing huge volume fluctuations during the NPT sampling. The integration algorithm became instable, forbidding any further analysis. Looking at this metastable melting line, it is clear that its slope does not

continue to decrease with increasing pressure as in the stable region; thus, the hypothesis of an hidden maximum appears to be rejected.

The slope of the diamond melting line is consistent with the only experimental point available [11] (see Fig. 1.5). When compared to the diamond melting line of the Brenner model [21], the LCBOPI$^+$ diamond melting line has a steeper slope yielding significantly higher temperatures for the diamond melting line.

1.4.3 Diamond Melting According to LCBOPII

We have not carried out an extensive numerical evaluation of the phase diagram as predicted by the LCBOPII. Yet, using direct free-energy difference calculations starting from the diamond melting line of the LCBOPI$^+$, we determined one point and the slope at that point of the diamond melting line for the LCBOPII. We sampled with the LCBOPI$^+$ a liquid and a diamond sample at the same phase point on the calculated diamond melting line and at intervals a virtual swapping between the two potentials, LCBOPI$^+$ and LCBOPII, was performed. This means that the energy of independent configurations during this run was evaluated also with the LCBOPII. We chose $T_m = 6{,}000$ K, which gave $P_m = 59.44$ GPa for the coexistence for the LCBOPI$^+$. We found for LCBOPII $T_m = 5{,}505$ K at the same pressure. The slope of the melting line was evaluated by means of the Clausius–Clapeyron equation. We found a slope of 28.04 K/GPa. We compare it to the very close value of 28.97 K/GPa as given by the LCBOPI$^+$ at the same pressure. Thus, by means of this single point evaluation, we found that LCBOPII has a melting line at lower temperature than the LCBOPI$^+$, but the slope should be similar between the two potentials.

1.4.4 Recent Developments

Recently, the melting curve of diamond in a range up to 2,000 GPa has been studied by ab initio MD simulations using density functional theory. Wang et al. [48] determined the relative stability of the diamond and liquid phase by evaluating the free energy of both phases. Correa et al. [26] determined the melting temperature using a "two phase" simulation method, where the system initially consists of a liquid and a diamond structure that are in contact. Subsequently the melting temperature is estimated by locating the temperature at which the system spontaneously evolves towards a liquid or a crystalline structure. In both ab initio MD studies it was found that the diamond melting curve shows a maximum; around 450 GPa [26] or 630 GPa [48].[4] Subsequent laser-shock experiments [49] provided data consistent

[4] The difference between these two values gives a hint on the uncertainties related to the two different methods used for calculating coexistence, given that the DF-MD set-up is quite similar in the two works.

with this observation, indicating a negative melting slope most probably in the region of 300–500 GPa. When comparing the LCBOPI$^+$ diamond melting curve, that monotonically increases with pressure, to the ab initio MD results of Refs. [26, 48] we see a significant deviation from 200 GPa onwards. This might be attributed to an incorrect description of the liquid structure at high compression. Indeed, LCBOPI$^+$ has not been validated against high density structures with coordination beyond four. These are typical configuration that might become more dominant in the pressure region beyond 200 GPa.

1.5 The Nature of Liquid Carbon: Absence of a *First-Order* Liquid–Liquid Phase Transition

In this section we re-examine the issue of the liquid–liquid phase transition (LLPT) for carbon. A short review of the relevant findings is given in Section 1.5.1. In Section 1.5.2 we describe the liquid at 6,000 K as predicted by several bond order potentials (see Fig. 1.9 for the complete list) and compare the results with density functional (DF) based molecular dynamics (MD) calculation. The temperature was chosen to agree with the DF-MD based analysis of the liquid Wu et al. [22] There the isotherm at 6,000 K was originally chosen for two reasons. Firstly it is expected to be far from coexistence in the density interval studied; this assumption is based on the phase diagram calculated by Glosli and Ree [21] using one of the Brenner bond order potential [35] (the authors do not specify which parameterization they use). Secondly, the 6,000 K isotherm is predicted by Glosli and Ree [20], with the BrennerI [35] bond order potential, to cross the liquid–liquid coexistence line. In Section 1.5.3 the analysis will be extended at all the relevant regions of the phase diagram, with the aim of ruling out the presence of a LLPT, at least within the scope of the LCBOP family. Intriguingly, signatures of a LLPT transition are nonetheless hinted at by LCBOPII for the strongly undercooled liquid, where the liquid would be anyhow dynamically arrested into a glass (see Section 1.5.2.3). A characteristic that carbon would share with water.

1.5.1 A Short History of Carbon LLPT

An Analysis of Experimental Data The possibility of a liquid–liquid phase transition (LLPT) in liquid carbon has been firstly investigated by Korsunskaya et al. [17], analyzing data on the graphite melting line proposed by Bundy [8] (those data showed a maximum melting temperature at 6.5 GPa). By fitting the data from Bundy into the original two levels model of Kittel [50] and postulating the existence of two liquids, Korsunskaya et al. found the critical temperature T_c of the LLPT. The

model is fitted with three points on the graphite melting line, with the respective derivatives, and with the heat of melting at a selected pressure. The authors assume that:

1. Liquid and solid have different compressibilities.
2. The nature of liquid carbon is described univocally by the relative fraction of the two liquids.
3. Each of the two liquids presents a volume change on melting, heat of melting and entropy of melting that are independent of T, P, and the fraction s: the volume change upon melting for the liquid is a linear combination of the volume changes of the pure species (i.e. for $s = 0, 1$), while heat and entropy of melting combine according to the regular solution rules.
4. The overall entropy jump on melting is independent of T (that is equivalent to assuming the same heat capacity in the liquid and the solid).

The fitting procedure gives an estimate for the critical pressure of ∼6.5 GPa and for the critical temperature of the searched transition at 3,770 K, i.e. below the melting temperature. The fitted value for the entropy of melting is the same for the two liquids, thus implying a vertical slope ($\mathrm{d}T/\mathrm{d}P$) of the coexistence line (in the metastable liquid region just below the critical temperature).

When the slope of two out of the three coexisting line meeting at a triple point is known, the slope of the third is also determined. On the basis of their results, the authors were thus able to calculate also the diamond melting line: they predicted it to have a negative slope. Note that the slope of the *graphite* melting line, and the slope of the diamond/graphite coexistence, as extracted from Bundy's data [7, 8], together with the densities of the phases obtained by fitting to the two levels model *implied* (via Clausius–Clapeyron equation) a negative slope of the diamond melting line. Different values of the slopes of the graphite boundary lines, and of the densities of the phases can yield rather different slope of the diamond melting line, as we have shown in Section 1.4.

Consistently with the slope of the fitted graphite melting line, the low density liquid (LDL, $s = 0$) is less heavy, and the high density liquid (HDL, $s = 1$) is heavier than the coexisting graphite. The nature of the two liquids is predicted as follows: at low pressure graphite melts into a liquid of neutral particles, which interact predominantly through dispersion (London) forces. Upon increasing pressure[5] the liquid metallizes into a close packed liquid. No assumption is made on the local structure.

A Semi-empirical Equation of State The modern discussion on the LLPT for carbon, starts with the elaboration of a semi-empirical equation of state for carbon, valid also at high P and T, by van Thiel and Ree [18, 51]. The equation of state is constructed on the basis of experimental data and electronic structure calculations. It is postulated the existence, in the graphite melt, of a mixture of a threefold (sp_2) and

[5] The transition in the stable liquid region is supercritical, thus continuous, but taking place in a short range of pressures around 6.5 GPa.

a fourfold (sp_4) liquid. The model of *pseudo-binary mixture* is assumed to describe the mixing of the two liquids [52]; the mixing energy J of the two liquids is written as: $\beta J = \left[A_0/\left(1 + (P/P_0)^{3/2}\right)\right] s(1-s)$ where $\beta = 1/(k_B T)$, A_0 and P_0 are fitting parameter, and s is the fraction of the sp_3 liquid. The value of these fitting parameters is essential to determine the possibility of the occurrence of a first order transition. Van Thiel and Ree show that fitting A_0 in order to obtain the graphite melting points of Bundy [8], the slope of the graphite melting line predicted by their model inverts its sign discontinuously in correspondence of the maximum, so that a first order LLPT arises. On the other hand, if they fit to the data from Ref. [9], the value of A_0 decreases so that the T_c of the LLPT drops below the melting line and the transition between the two liquids becomes continuous in the stable liquid region. As pointed out by Ponyatovsky [53] the expression for βJ proposed by van Thiel and Ree involves two ambiguities. Firstly, extrapolating the coexistence line between the two liquids at atmospheric pressure, the coexistence temperature would be $T \sim 3{,}700$ K: this would imply that the sp_3 liquid (and the glass) would be more stable than the sp_2 at room pressure up to very high temperatures, which is in contrast to the experimental data. Furthermore, J is proposed to have a linear dependence on T, so that, when $T \to 0$, also the mixing energy would tend to zero, i.e. at zero temperature the regular solution would become an ideal solution. This is extremely unusual.

Experimental Suggestions from the Graphite Melting Line Togaya [16] found a maximum in the melting line at $P_{max} = 5.6$ GPa. The author fitted the six experimental points with two straight lines: with positive slope at pressures lower than P_{max}, with negative slope at pressures higher than P_{max}. The discontinuous derivative of the melting curve at the maximum would imply there a triple point graphite/LDL/HDL, as a starting point of a LLPT coexistence line.

Prediction of a Short Range Bond Order Potential In Ref. [20] Glosli and Ree reported a complete study of a LLPT simulated with the Brenner bond order potential [35] in its version with torsional interactions [36]. The authors simulated in the canonical (NVT) ensemble several samples at increasing densities at eight different temperatures. By measuring the pressure, they show the familiar van der Waals loop denouncing mechanical instabilities at certain imposed densities. Using the Maxwell equal-area construction, the authors calculated the LLPT coexistence line, ending in a critical point at $T = 8{,}802$ K and $P = 10.56$ GPa. The lowest temperature coexistence point was calculated at $T = 5{,}500$ K and $P = 2.696$ GPa. The LDL/HDL coexistence line should meet the graphite melting line at its maximum, but unfortunately the BrennerI potential does not contain non bonded interactions, thus it cannot describe neither bulk graphite nor its melting line. To overcome this deficiency, the authors devised an ingenious perturbation method. Assuming constant slope of the negative sloped branch of the graphite melting line[6] and fixing the

[6] The authors adopted the graphite melting line measured by Togaya [16]. This melting line is reported in Fig. 1.4, together with our results. According to Glosli and Ree, from the maximum of that melting line would branch off the LLPT coexistence line.

graphite/diamond/HDL triple point at a value taken from the experimental literature, they give an estimate of the graphite/LDL/HDL triple point, at $T = 5{,}133\,\mathrm{K}$ and $P = 1.88$ GPa. The LDL was found to be mainly twofold (sp) coordinated with a polymeric-like structure, while the HDL was found to be a network forming, mainly fourfold, (sp_3) liquid. Following the predictions of this bond order potential, the sp_2 coordinated atoms would be completely avoided in the liquid. The authors identified the reason in the presence of torsional interactions. In fact, the increase in density demands an increase in structures with higher coordination than the sp, which is entropically favored at low densities. Each bonds of the sp_3 structures can freely evolve around the bond axis, while bonds between sp_2 sites are constrained in a (almost) planar geometry by the torsional interactions: this implies a low entropy for a liquid dominated by sp_2 sites. This low entropy would eventually destabilize the sp_2 sites towards the sp_3. To prove this conjecture, the authors calculated two relevant isotherms in the original version of the potential, without torsional interactions, finding no sign of a LLPT. Since some torsional interactions are definitely needed to mimic the double bond reluctancy to twist, the authors concluded that the LLPT predicted by the Brenner bond order potential with torsion is more realistic than its absence when torsional interactions are switched off.

Tight binding calculations [54] showed no evidence of van der Waals loops at some of the temperatures analyzed in Ref. [20]. As Glosli and Ree note, the tight binding model used in [54] is strictly two-center, thus the torsional interactions *cannot* be described.

An Ab Initio Confutation of the LLPT In Ref. [22], Wu et al. reported on a series of NVT-CPMD simulations at 6,000 K from density $1.27 - 3.02 \times 10^3$ kg/m^3, in a range where the BrennerI potential showed the first order LLPT at the same T. No sign of a van der Waals loop was found: in contrast to the BrennerI results of the previous section, two approaching series starting from the lowest and the highest density, were found to meet smoothly at intermediate densities. Looking for the reasons of the failure of the BrennerI potential, the authors calculated, with the same density functional (DF) used in the CPMD simulations, the torsional energy of two model molecules. One, $(CH_3)_2CC(CH_3)_2$ (see Fig. 2 in Ref. [30] for a schematic representation), was chosen so that the bond between the two central atoms represents a double bond in a carbon network: two sp_2 sites are bonded each to two sp_3 sites; the peripheral hydrogens are needed to saturated the sp_3 atoms and are intended to have no effect on the central bond. The second molecule, $(CH_2)_2CC(CH_2)_2$ (see again Fig. 2 in Ref. [30] for a schematic representation) is a portion of a completely sp_2 coordinated network: in the bond order language, the central bond is conjugated. The two molecules were geometrically optimized in their planar configurations and then twisted around the central bond axis in steps of $\pi/12$. In each configuration the electronic wave function was optimized, without further relaxations, to give the total energy, that was compared to the planar configuration total energy. The difference is the torsional energy. The DF calculations found a surprising picture (see Section 6.7 in Ref. [40] or Fig. 3 in Ref. [30]): while the double bond torsional energy was only slightly overestimated by the BrennerI potential

at intermediate angles, the DF torsional energy for the conjugated bond showed a completely different scenario compared to the classical prediction. It shows a maximum at $\pi/4$, while the planar and orthogonal configuration have basically the same energy. For the BrennerI potential, the torsional energy in this conjugated configuration is monotonically increasing with the torsion angle, just as for the double bond configuration. On average, considering that the conjugated configuration would be characteristic of a mainly sp_2 coordinated liquid, the torsional interactions are enormously overestimated by the classical potential. As a further proof, the authors tried to lower torsional energy of the conjugated bond in the classical potential, by tuning the proper parameter, and found a much less pronounced LLPT. Note that the functional form of the torsional interactions for the BrennerI potential *cannot* reproduce the DF data here mentioned. Wu et al. concluded: "Brenner potential significantly overestimates the torsional barrier of a chemical bond between two- and three-center-coordinated carbon atoms due to the inability of the potential to describe lone pair electrons"; and: "Brenner potential parameters derived from isolated hydrocarbon molecules and used in the literature to simulate various carbon systems may not be adequate to use for condensed phases, especially so in the presence of lone pair electrons". The bond-order (Brenner like) potential (LCBOPI$^+$) [29] incorporates a much more flexible and transferable definition of the torsional interactions. In Section 1.5.2 we will show that the conclusion of Wu et al. is not necessarily true for all BOPs; we will show how our definition of the torsional interaction is able to reproduce relevant features of liquid carbon, as described by density functional based molecular dynamics.

1.5.2 Properties of Liquid Carbon, According to Selected BOPs

1.5.2.1 Computational Methods

We performed Monte Carlo (MC) simulations of 128 particles in a cubic box with periodic boundary conditions with all the bond order potentials we chose for the comparison. We sampled at 6,000 K the constant volume (NVT) ensemble for densities smaller than 2.5×10^3 kg/m^3 and the constant pressure (NPT) ensemble for larger densities where the increase of pressure is steeper, with an overlap between the two regions to check for consistency. The pressure in the NVT simulation for the BOPs was calculated without virial evaluation, by means of virtual volume rescaling [55, 56].

We performed constant volume DF-MD simulations using the Car–Parrinello method [57] as implemented in the CPMD package [58]. The system consisted of 128 atoms in a cubic box with periodic boundary conditions at nine densities and a temperature $T = 6{,}000$ K, imposed by means of a Nosé–Hoover [59] thermostat. We used the Becke [60] exchange and Perdew [61] correlation gradient corrected functional (BP) with a plane wave basis set cut off at 35 Ry and sampled the Brillouin zone only in the gamma point. BP gives a correct description of bulk

diamond. Each state point was studied for 5 ps, starting from a sample equilibrated via the LCBOPI$^+$; only minor structural changes occurred in the first tenths of ps. Since liquid carbon is metallic, we imposed a thermostat for the electronic degrees of freedom in order to ensure a proper implementation of the Car–Parrinello scheme [62].

1.5.2.2 Radial Distribution Functions

In Fig. 1.6 we present the radial distribution functions ($g(r)$) obtained for the LCBOPII, LCBOPI$^+$, and DF-MD at four selected densities along the 6,000 K isotherm. Taking DF-MD as a reference, we see that the LCBOPII is a major improvement with respect to the LCBOPI$^+$. In particular the minimum between the first and second shell is now properly described. Here we should note that the radial distribution functions and the coordination fractions, at $\rho = 3.75 \times 10^3$ kg/m^3 were used as a test system in the development of the potential.

The figures also show that the LCBOPII reproduces the DF-MD values for the peak positions, and the height of the second and third peak. Only the fist-peak height is slightly overestimated by the LCBOPII, consistent with the fact that the LCBOPII showed larger values for the higher coordination numbers (Fig. 1.14).

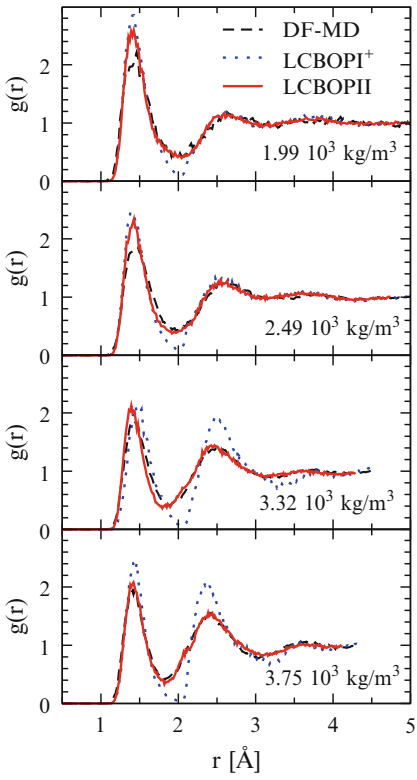

Fig. 1.6 Comparison of the radial distribution functions at 6,000 K and four selected densities between the LCBOPII (*solid lines*), the LCBOPI$^+$ (*dotted lines*), and the reference data taken from our own DF-MD simulations (*dashed lines*)

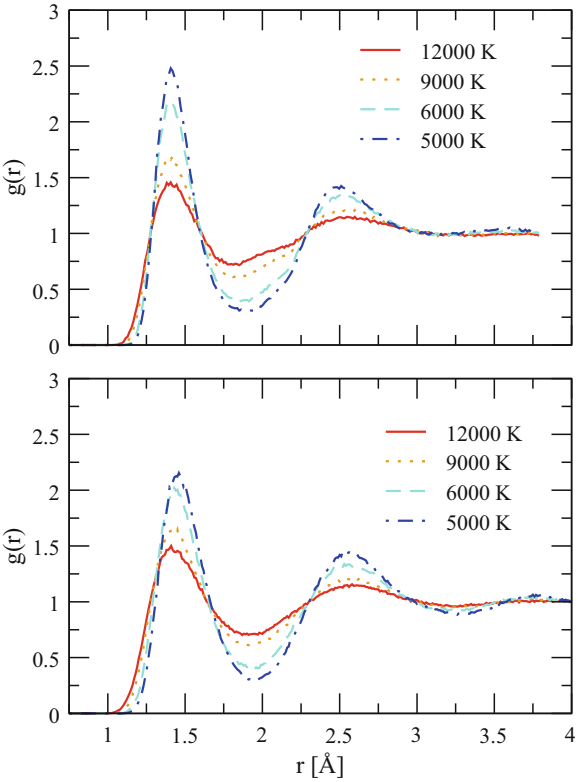

Fig. 1.7 Comparison of the radial distribution functions at 2.9×10^3 kg/m^3 and four temperatures between the LCBOPII (*top panel*) and reference data taken from Ref. [63] (*bottom panel*). *Solid lines* are at 12,000 K, *dotted lines* at 9,000 K, *dashed lines* at 6,000 K, and *dotted–dashed lines* are at 5,000 K

Figure 1.7 compare the LCBOPII radial distribution functions for a liquid at 2.9×10^3 kg/m^3 at four different temperatures with 64-atom DF-MD data from Ref. [63], calculated using the local density (LDA) functional. This figure makes clear that, up to 12,000 K, also the temperature dependence is well reproduced by the LCBOPII. The temperature dependence is typical for a liquid: the peak heights decrease with increasing temperature, while minima increase, indicating a gradual loss of structure. It is striking that all the curves cross at the same points at $g(r) = 1$. In fact, at $\sim$0.165, $\sim$0.230, and $\sim$0.285 nm, the value of $g(r)$ is 1, regardless of the temperature.

Angular Distribution Function In Fig. 1.8 we show the comparison of the angular distribution functions between LCBOPII and DF-MD calculations at the same densities as for the radial distribution function (see Fig. 1.6). The overall agreement is impressive also in this case. The position of the main peak together with its broadness agrees at all densities. Compared to the LCBOPI$^+$, this is a significant

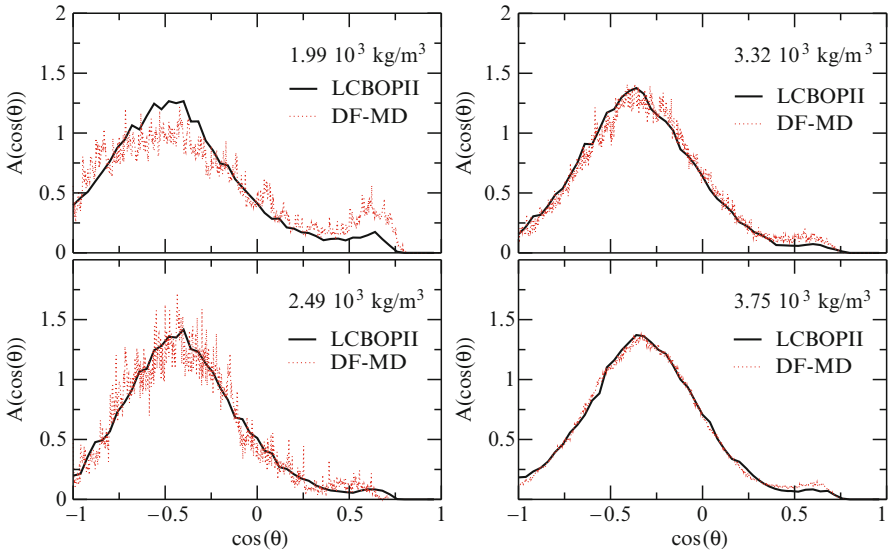

Fig. 1.8 Angular distribution functions at 1.99 (*top left panel*), 2.49 (*bottom left*), 3.32 (*top right*), and 3.75×10^3 kg/m^3 (*bottom right*), and $T = 6{,}000$ K; we compare DF-MD (*dotted lines*) with the LCBOPII (*solid lines*)

improvement as the results of Ref. [47] showed that there was only a qualitative agreement between the LCBOPI$^+$ and DF-MD, with the LCBOPI$^+$ underestimating the presence of sub 90 degrees structures. The improvement of the LCBOPII over the LCBOPI$^+$ should be attributed to the softening of the angular part in the potential yielding a lower energy for fourfold coordinated structures at small angles. As for the radial distribution functions, the major discrepancies are at lower densities: in this case the position and/or the broadness of the secondary peak at low angles is only qualitatively reproduced.

1.5.2.3 Equation of State

Figure 1.9 shows the equations of state of all the mentioned potentials. All the points were calculated by us, except for the AIREBOII potential [38] points in the bottom panel, that come from Ref. [39], and the DF-MD data of Wu et al., marked with PBE (see below). The data from Ref. [22] are calculated with a different functional (i.e. PBE, as labelled in Fig. 1.9) and a different cut-off energy (50 Ry). In view of the relatively low cut-off energy (35 Ry), we had to correct the pressures for the spurious contribution due to Pulay forces [64]. In the density range where we can compare with the results of Wu et al. [22], the pressures that we compute are some 15% lower than those reported by Wu et al. The difference in calculated pressures between the two DF-MD simulations should be attributed to the use of a different functional. Different plane-wave cutoffs and pseudopotentials should not contribute

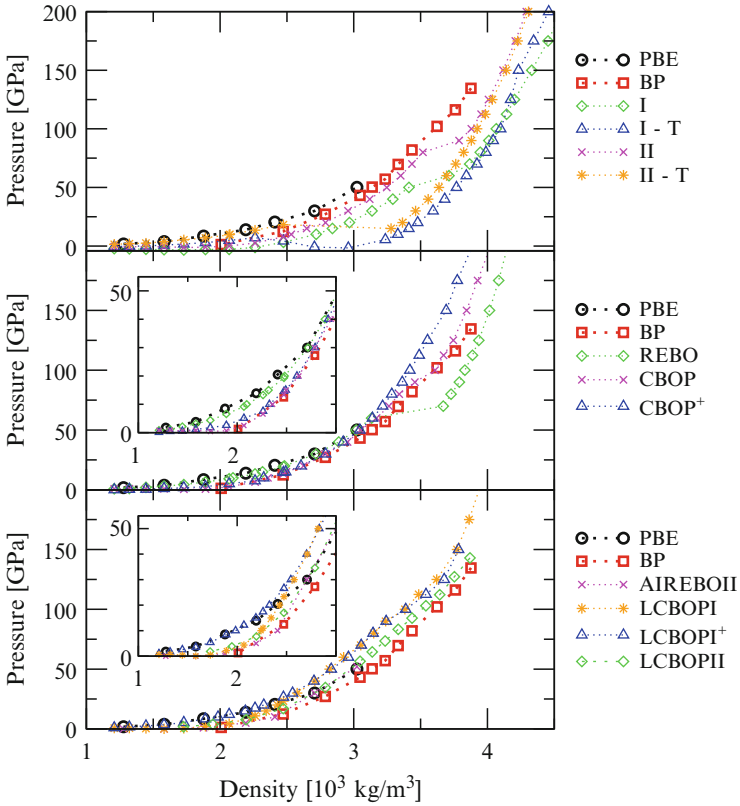

Fig. 1.9 Equations of state at $T = 6{,}000$ K for all the potentials tested. The abbreviation 'PBE' and 'BP' refer to two types of gradient corrected density functionals (see text), and are taken as reference data in these plots. The Brenner potentials are labelled 'I' and 'II' for their original version [35], i.e. without torsional interaction, and 'I-T' and 'II-T' for the version [36] with added torsional interactions. The REBO potential is presented in Ref. [37]: the data points come from our simulations. The CBOP is presented in Ref. [27]; with CBOP$^+$ is labelled the CBOP with modified angular interactions and added torsional interactions, in the same way as for the LCBOPI$^+$, but with appropriate parameters. LCBOPI [27], the LCBOPI$^+$, and the LCBOPII are presented in Refs. [29,40]. The AIREBOII potential is a slight modification of the AIREBO potential [38]; it is described in Ref. [39] (the data points shown here are taken from the same reference)

significantly to this discrepancy, when one considers that both setups yielded good binding energies. We have checked that our samples were indeed liquid: over the whole isotherm we have observed diffusive behavior in both the MC-LCBOPI$^+$ and the DF-MD simulations, the latter indicating a self-diffusion coefficient at least of order 10^{-5} cm^2/s.

The two series of DF-MD data are taken as reference, and for this reason repeated in each panel. The original Brenner potentials [35], BrennerI and BrennerII, with and without torsional interactions [36], are in the top panel. The center panel is for the subsequent generation of *short range potentials*: REBO [37] and CBOP [27].

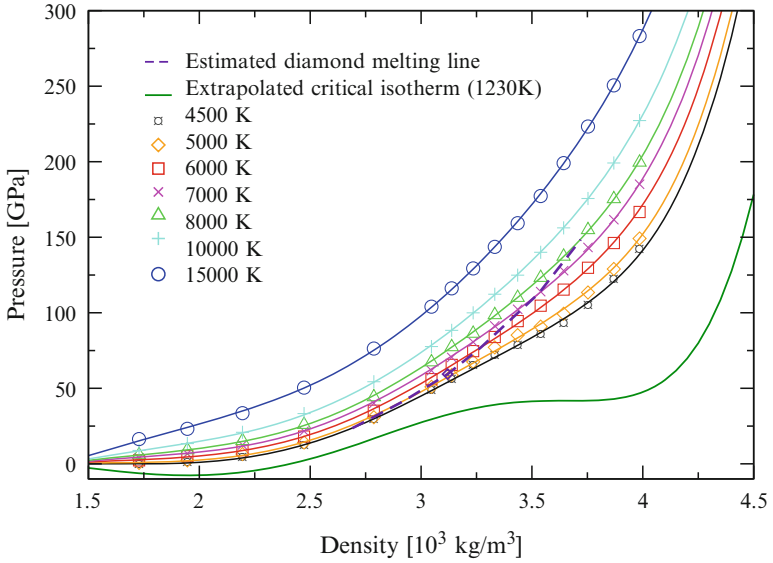

Fig. 1.10 Equations of state for the LCBOPII at seven different temperatures. *Error bars*, not shown, are within the symbol size. The relative error is around 1% at the highest pressure and increases up to 10% at the lowest (i.e. smaller than 5 GPa). The *thick line* at the bottom is the extrapolated critical isotherm, at 1,230 K. It has a horizontal inflection point at density 3.66×10^3 kg/m^3 and pressure 41.74 GPa. The *dashed line* is the estimated *diamond melting line*, started from the calculated point shown as a diamond (at 5,505 K, 59.4 GPa, and 3.12×10^3 kg/m^3, see previous section), and extrapolated assuming constant $\mathrm{d}T/\mathrm{d}P$

With *short range potential* we mean a potential which includes only covalent interactions. We label with CBOP$^+$ the CBOP with modified angular interactions and added torsional interactions, in the same way as for the LCBOPI$^+$. The bottom panel groups the potentials with non-bonded interactions: AIREBOII, LCBOPI and LCBOPI$^+$. The bottom panel also shows the equation of state as given by the LCBOPII [29].

In Fig. 1.10 we have plotted the pressure–density curves for 7 isotherms. Figure 1.11 shows the equation of state surface, fitted to data coming from 7 isotherms, each sampled at 15 densities. In Fig. 1.10 also the estimated coexistence line is plotted. In the stable region all curves show a regular monotonic increase of the slope of the curve. In the undercooled region we observe for the 4,500 and 5,000 K isotherms, in a small density region around 3.3×10^3 kg/m^3, a decrease of the slope. For the LCBOPI$^+$, this wiggling of the pressure–density curve was a pronounced feature at 6,000 K, and associated with a rapid switching of the dominant coordination from three- to fourfold. For the LCBOPII, the same coordination change occurs in the wiggling region around 3.3×10^3 kg/m^3 of the 4,500 and 5,000 K isotherms (see below).

A wiggle in the $\rho - P$ equation of state denounces a sudden decrease of the isothermal compressibility ($1/\rho \ \mathrm{d}P/\mathrm{d}\rho$). Thinking pressure as the leading

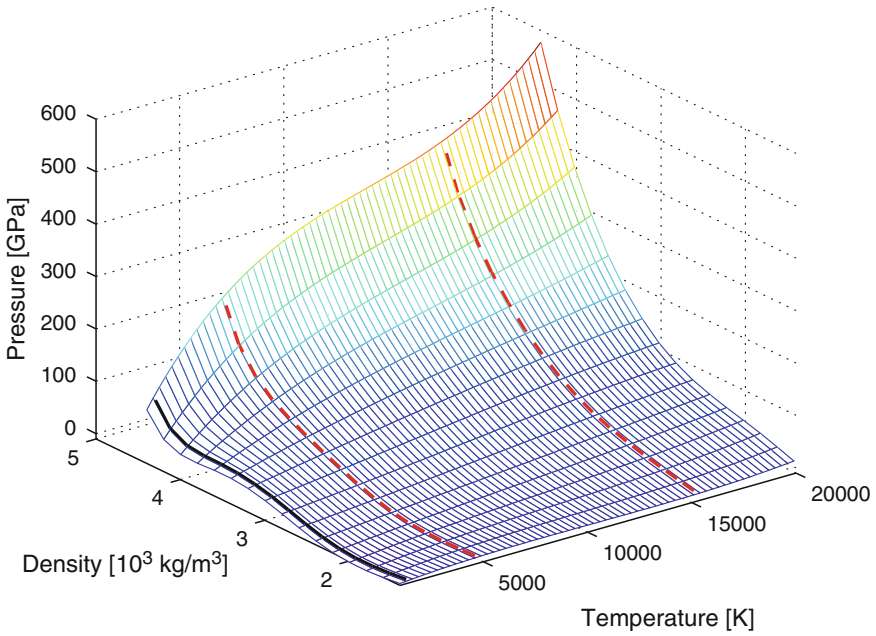

Fig. 1.11 Three dimensional density–temperature–pressure plot of the fitted equation of state for LCBOPII, $P = P(\rho, T)$. The *solid line* is the (deeply supercooled) critical isotherm (at 1,230 K), while the two *dashed lines* are the two extreme isotherms of the simulated state points (i.e. 4,500 and 15,000 K)

parameter, in this region the liquid reacts to an increase of pressure with an increase of density, higher than at the surrounding densities. This is understandable thinking that on the left and on the right of the wiggle, the liquid needs mainly to shorten covalent bonds to increase density. In the transition region, a bigger increase of density is readily achieved by receiving an extra neighbor. Given the shape of the equation of state at lower temperatures, nothing would prevent to speculate the existence of a liquid–liquid phase transition at even lower temperatures, if ever a first order one. We observed that samples at temperatures lower than ∼4,000 K rather freezed, especially at densities higher than 3×10^3 kg/m^3. This makes the speculation impossible to prove with this sample size.

In Ref. [65], we proposed a 19 parameters fit for the Equation of State for LCBOPII. The polynomial fit reproduced the wiggling of the 4,500 and 5,000 K isotherms for the undercooled liquid. Extrapolating the fit at low temperatures, inaccessible in the liquid phase with our system size, the wiggles become more pronounced, yielding an inflection point with zero slope in the $P - \rho$ plane for the 1,230 K isotherm at 3.66×10^3 kg/m^3, and 41.74 GPa. This behavior is typical for the critical isotherm. At lower temperatures the isotherms of the fit function show a van der Waals loop, indicating a first-order phase transition associated with a density change. However, in our simulations the system freezes below 4,000 K, especially at densities higher than 3×10^3 kg/m^3. Hence it would be rather speculative to

propose the presence of a liquid–liquid phase transition. Still it might be interesting to explore the undercooled liquid by considering (much) larger system size and perform careful annealing to see if a scenario similar to that of liquid water, with its speculated liquid–liquid phase transition hidden in the glass region [66–68] would appear.

1.5.2.4 Coordination

The coordination fractions are shown in Figs. 1.12 and 1.13; for a clearer comparison, these figures share the same labelling criterion for the two-, three-, and fourfold

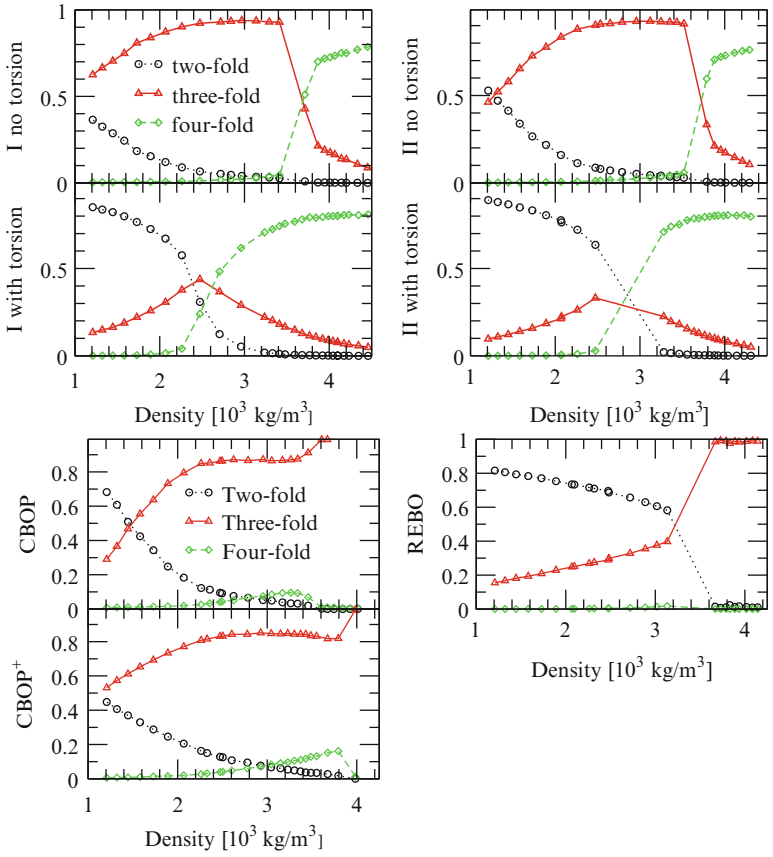

Fig. 1.12 *Top four panels:* coordination fractions at $T = 6,000$ K for the Brenner potentials of Ref. [35] (BrennerI and BrennerII, without torsional interactions) and Ref. [36] (BrennerI and BrennerII, with torsional interactions). *Bottom three panels:* coordination fractions at $T = 6,000$ K for more recent short range potentials [27,37], see text for the abbreviations. *Circles* are always for twofold, triangles for threefold, and diamonds for fourfold sites (atoms)

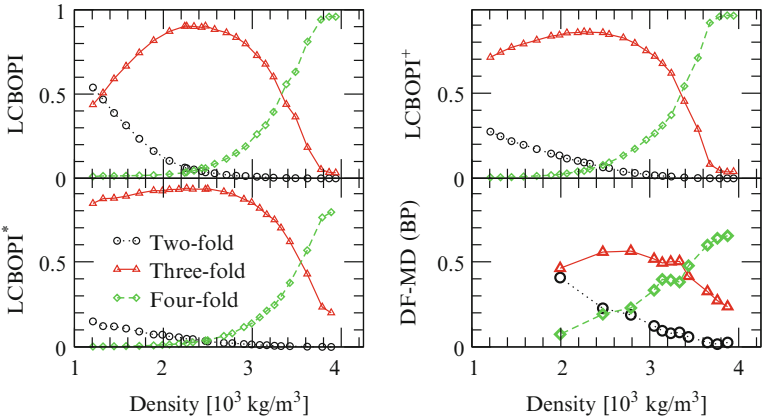

Fig. 1.13 Coordination fractions at $T = 6{,}000$ K for long range potentials (LCBOPI, LCBOPI*, and LCBOPI$^+$) before the introduction of LCBOPII (Refs. [27,40], see also text for the abbreviations). The density functional (BP) data are reported for comparison. The data for LCBOPI$^+$ and BP are shown in Fig. 1.14, too. *Circles* (*black*), *triangles* (*red*), and *diamonds* (*green*) indicate the fraction of two-, three-, and fourfold coordinated atoms, respectively

sites, and the same axes. For the AIREBOII potential no coordination data are available; 'LCBOPI*' (in Fig. 1.13) indicates an intermediate version of the LCBOPI$^+$, i.e. with the softened angular interactions at low coordination [40], but without torsional interactions.

Figure 1.14 shows the coordination fractions calculated with the LCBOPII, LCBOPI$^+$, and DF-MD along the 6,000 K isotherm. We see that, except for a slight overestimation of the threefold fractions in the low-density regime, the LCBOPII results reproduce the DF-MD data very well, both for the density dependence as for the absolute values. The LCBOPII improves the predictions of the LCBOPI$^+$: at densities up to $\sim 3.4 \times 10^3$ kg/m^3, the LCBOPII predicts less threefold and more two- and fourfold sites, thus getting closer to the DF-MD data. At higher densities, where the LCBOPI$^+$ overestimated the fourfold fraction, the coordination fractions predicted by the LCBOPII almost perfectly recover the DF-MD data. Fivefold coordinated atoms (not shown in Fig. 1.14) only appear in the high-density region. At 3.75×10^3 kg/m^3 the fraction for the LCBOPII is 0.1, slightly larger than DF-MD value of 0.07. Note that this is a remarkable achievement of the potential, as the structures used to develop the LCBOPII did not have fivefold coordination. We also note that in the high density range, short range BOPs hardly show coordination beyond three, while for the LCBOPI$^+$ the fivefold fraction remained negligible. The appearance of fivefold coordinated structures in LCBOPII calculations is due to the presence of the "middle range" part in the potential and to the softening of angular correlations. In fact, in older BOPs as well as in the LCBOPI, a small angle such as 60 degree had a significant energetic penalty, fitted to a 12-fold structure (i.e. an fcc lattice) that applied also for 5-fold sites. With the LCBOPII the penalty at small angle for this lower coordination has been reduced [29]. As already shown

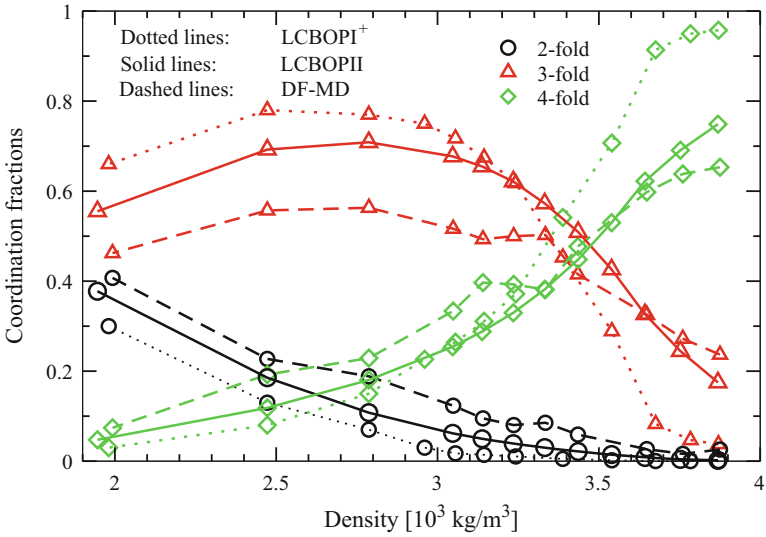

Fig. 1.14 Comparison of coordination fractions at 6,000 K between the LCBOPII (*solid lines*) and reference data coming from our own DF-MD (*dashed lines*). Data at density 2.79×10^3 kg/m^3 and higher are the same shown in Ref. [47]. *Circles* always represents twofold sites, *triangles* threefold, and *diamonds* fourfold. Fivefold sites are not shown but can be deduced by subtraction, since no atoms with a single bond (onefold) or sixfold sites were observed at these densities. The *error bars*, not shown, are within the symbol size, ∼0.01 for the LCBOPII, and ∼0.02 for the DF-MD points

in Ref. [47] the REBO potential yields a negligible fourfold fraction at all the densities: the threefold atoms replace the twofold upon increasing density, until the spurious LLPT at which all the atoms become threefold. The transition is also appears for CBOP, but the fraction of fourfold atoms raises until ∼10% before the transition. We mention that the environment dependent potential (EDIP) introduced by Marks [69] is similar to the LCBOPII in reproducing the DF-MD coordination fractions at 5,000 K [70].

In Fig. 1.15 we show the average coordination fractions for the LCBOPII at seven temperatures. Onefold coordinated atoms appear only in a small amount (a few %) at the lowest densities, and are not shown. Considering the density dependence, we observe that, for all temperatures, the atoms are mainly two- and threefold coordinated in the low density region, with the twofold sites gradually replaced by three- and fourfold sites upon increasing density. At 6,000 K the two- and threefold fractions match around $\rho = 1.73 \times 10^3$ kg/m^3. Note that the maximum of the threefold fraction is at $\rho \sim 2.75 \times 10^3$ kg/m^3 for all temperatures. Beyond this density the dominant coordination is three- and fourfold. The threefold sites are replaced by fourfold sites over a relatively short density range around $\rho = 3.4 \times 10^3$ kg/m^3. The fivefold fraction only appears with a significant fraction in the high-density region and shows a marked temperature dependence. This also implies a stronger temperature dependence of the fourfold fraction in the high-density region.

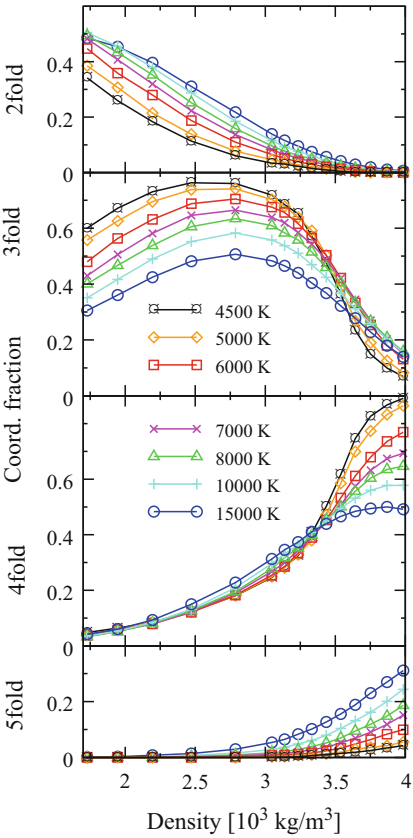

Fig. 1.15 Coordination fractions at seven temperatures according to the LCBOPII. The fraction of sixfold coordinated atoms were negligible at all simulated state points. Each panel shows a different coordination fraction interval but y-axes share the same unit, so that they can be directly compared. The *error bars*, not shown, would be smaller than the symbol size, typically around 0.01

1.5.2.5 Discussion

Looking at all the equations of state and coordination fractions, BrennerI and BrennerII with torsional interactions show the LLPT from a mainly twofold to a mainly fourfold liquid, as discussed in Section 1.5.1. We show that also for the version without torsional interactions, the potentials present an abrupt transition from a mainly threefold to a mainly fourfold liquid from density 3.4–3.8 $\times 10^3$ kg/m^3. The REBO potential displays a quite good reproduction of the DF-MD *equation of state* at lower densities (up to 3.2×10^3 kg/m^3), but, also at low density, the structure of the liquid is far from the reference data (see Fig. 1.13, bottom right panel): twofold atoms are predominant where DF-MD predicts threefold to be. Furthermore, the liquid undergoes a LLPT at 3.2×10^3 kg/m^3. The high density liquid is revealed to be, upon visual inspection of the snapshots, a completely threefold graphite-like liquid consisting of almost defect-less sliding sheets that eventually get stuck upon further increasing of the pressure. We note that the transition occurred regularly upon compression for different, independent, samples. Note that the fourfold fraction remains always negligible. Also the CBOP and the CBOP$^+$ present this spurious transition,

but the predominance of threefold sites in the lower density regime is correctly given by both these potentials. Note that the equation of state of CBOP is the one in better agreement with our DF-MD data. Nonetheless, as it is dramatically shown by the coordination fractions, a good equation of state is not sufficient to assess the accuracy of a potential.

With the introduction of non-bonded interactions, the fraction of fourfold becomes eventually non negligible at higher densities. For these potentials, the coordination fractions depict a similar scenario at high density, whereas the main differences are found at intermediate densities. The original potential, LCBOPI, predicted a too stiff variation of the threefold fraction, both when increasing, substituting the twofold predominance, and when decreasing, substituted by the fourfold sites. The introduction of softened angular correlation for low coordinated atoms, the case of LCBOPI*, increased the stability of the threefold sites versus two- and fourfold sites. The introduction of torsional interactions, i.e. LCBOPI$^+$, yielded a picture closer to the reference data. Anyway the agreement remains qualitative since only the trends and the fold-type of dominant coordination is reproduced, while the absolute values are always shifted towards overestimation of the dominant fraction.

DF-MD predicts a marked switching of dominant coordination from three to four around 3.4×10^3 kg/m^3. Judging from the isotherm of Fig. 1.9, the transition seems to be continuous with no sign of a van der Waals loop. These results are consistent with the tight binding MD simulations of Ref. [54]. In contrast, between 3.3 and 3.6×10^3 kg/m^3, where the switch of dominant coordination takes place, the MC results based on the LCBOPI$^+$ display large fluctuations in density at the imposed pressure of 100 GPa, resulting in a slight bending of the isotherm of Fig. 1.9.

Our results provide no evidence of a first-order transition but rather indicate a pronounced but continuous change of dominant coordination.

It is rather surprising that the LCBOPI$^+$ potential reproduces the transformation to a predominantly fourfold coordinated liquid, while the REBO potential does not. The latter is in fact a potential known to give rather accurate predictions in several environments [37]. The high temperature liquid is, anyway, the most demanding benchmark for a semiempirical potential, due to the presence of a large variety of local structures. It thus becomes crucial to have a reasonable estimate of the interaction energy for configurations that are very far from cluster and lattice structures in their minimum energy. Apparently, the isotropic long-ranged interactions play a crucial role in stabilizing the high density liquid. This behavior is rather puzzling as long-ranged interactions were predicted (see, e.g., Ref. [21]) to play a negligible role at these high densities. It has to be recognized that the Brenner original potentials, even without torsional interactions, present at a certain density the switch to the dominant fourfold coordination, but with a strongly first order LLPT, that is as spurious as the one predicted by the torsional interaction corrected versions.

Finally, we note that long-ranged interactions were introduced in Ref. [27] to describe threefold coordinated graphitic phases, and no attempt was made to make the long range interactions dependent on the local environment. Torsional interactions appear to be important, since, without them, the calculated pressures would be too

high for high densities and too low at low densities. We conjecture that the combination of torsional interactions, and long range forces is required to give the best description of the liquid.

1.5.3 No Liquid–Liquid Phase Transition in the Stable Liquid Region

In Section 1.4 we reported the calculation of the phase diagram according to the LCBOPI$^+$. With the knowledge of the full melting lines, we can state that there is no LLPT in the stable liquid phase. One indication is the smoothness of the slopes of the melting lines. A further argument lies in the structure of the liquid near freezing. We determined several structural properties of the liquid at coexistence with the solid phases (the properties were calculated during the same simulations of the state points needed for the Gibbs–Duhem integration of the previous section). Figure 1.16 shows the coordination fraction in the liquid along the coexistence lines with graphite and diamond. Since the coexistence lines are unimodal, the graph can be shown indifferently with density, pressure, or temperature on the horizontal axis. We chose to plot the graph with a linear scale in density. The dashed line is the graphite/diamond/liquid triple point. On the left hand side of the triple point, the liquid coexists with graphite, while on the right hand side it coexists with diamond. The threefold and twofold coordination fractions remain rather constant when the

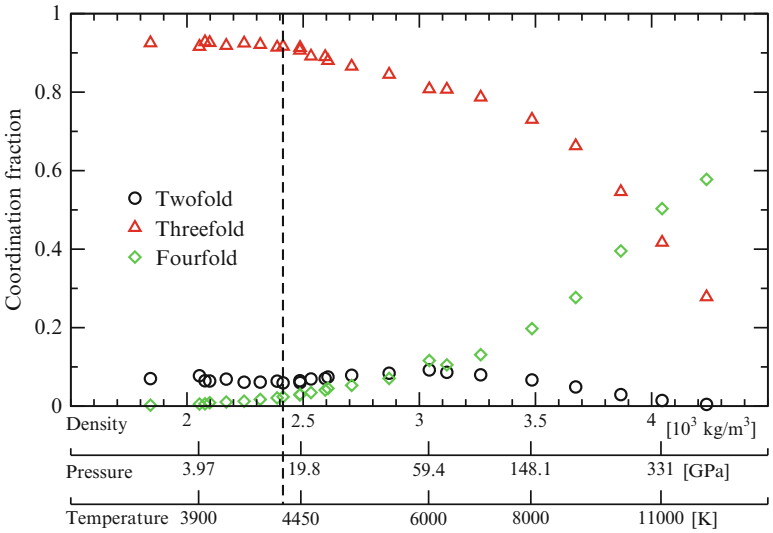

Fig. 1.16 Coordination fraction of the liquid along the *melting line(s)*, according to LCBOPI$^+$. The *melting lines* are unimodal, thus the fixing of ρ fixes also P and T. We arbitrarily chose the ρ scale to be linear. The *dashed line* marks the liquid/graphite/diamond triple point

liquid coexists with graphite, with the fourfold slightly increasing, to account for the increase in density. Along the diamond melting line, on the right hand side of the dashed line, the threefold coordinated atoms are gradually replaced by fourfold coordinated atoms. However, only at (3.9×10^3 kg/m^3, 300 GPa, and 10,500 K) the liquid has an equal fraction of threefold and fourfold coordinated atoms. The change of dominant coordination is rather smooth; moreover, it is fully reversible, without signs of hysteresis, in the region around the swapping of dominant coordination. These results contradict the generally assumed picture (see e.g. Ref. [18]) that diamond melts into a fourfold coordinated liquid.

The interrelation between three and fourfold sites, was further investigated by calculating the partial radial distribution functions ($g_{ij}(r)$) of the liquid at 300 GPa, and 10,500 K. Partial radial distribution functions are defined as the probability of finding a j-fold site at a distance r from a i-fold site[7]; the total radial distribution function g is recovered by: $g = \sum_i g_{ii} + 2\sum_{i \neq j} g_{ij}$. We show the results in Fig. 1.17; we focus on the three predominant curves, describing the pair correlations between threefold atoms (g_{33}), between fourfold atoms (g_{44}), and the cross pair correlation between three- and fourfold sites (g_{34}). Disregarding the rather pronounced minimum in correspondence of the dip around 2 Å of the g_{33} and the g_{34}

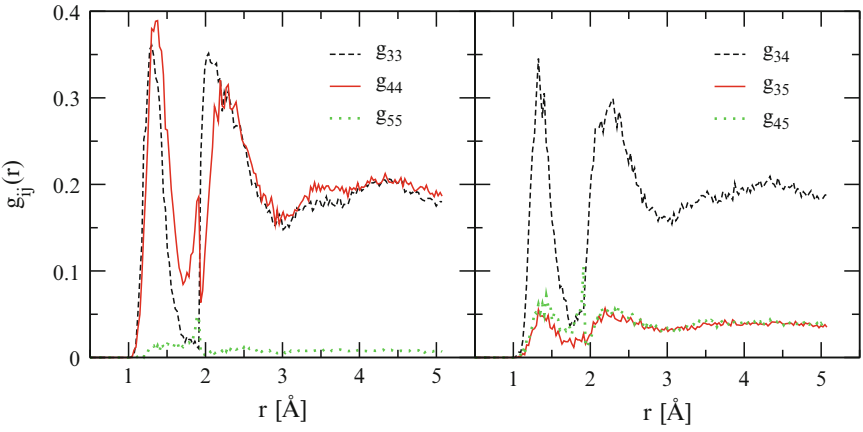

Fig. 1.17 Partial distribution functions g_{ij} of the LCBOPI$^+$ liquid at 10,500 K and $\sim$ 300 GPa, where the liquid coexists with diamond and three- and fourfold atoms are equally present (i.e. where the *dotted line* with cross symbols in Fig. 1.5 cuts the *diamond melting line*) . The left panel is for the diagonal contributions (i.e. for $i = j$), while the right panel is for the cross correlations (i.e. for $i \neq j$)

[7] The factor two multiplying the off-diagonal partial distribution functions ($g_{ij}(r)$, with $i \neq j$) is needed when those distributions are calculated according to the literature (e.g. Refs. [71, 72]). The algorithm calculating the $g_{ij}(r)$ browses the pairs of particles only once, as is commonly done for the total $g(r)$. If the algorithm browsed over all the neighbors of each particle, the factor two would clearly not be needed.

(see introduction to Ref. [29] for a discussion of this problem), the similarity of three curves at all distances r is striking. The two sites (i.e. threefold and fourfold atoms) are almost indistinguishable: if there was a tendency towards a phase transition, one would expect some segregation of the two structures. In contrast, looking at distances within the first neighbors shell, a threefold site seems to bond indifferently to a three- or a fourfold site, and viceversa. Furthermore, the partial structures up to the third, quite pronounced, peak at $\sim$4.5 Å, are almost the same for these three partial radial distribution functions.

We determined the properties of the metastable liquid in the stable diamond region. Figure 1.5 shows the liquid $P - T$ state points (crosses) that exhibit an equal number of three and fourfold coordinated atoms. It ranges from high-pressure high-temperature region where the liquid is thermodynamically stable down into the diamond region, where the liquid is metastable for the LCBOPI$^+$. The state point in which this line cuts the diamond melting line is the state point for which we plotted the partial radial distribution function g_{ij} in Fig. 1.17. In Fig. 1.5, the circles indicate state points in which the LCBOPI$^+$ liquid freezes in the simulation. Enclosed by the two set of points lies a liquid state point with a diamond-like structure liquid.[8] This suggests that a (meta)stable liquid with a dominantly fourfold coordination may only exist for pressures beyond $\approx$100 GPa and could imply that the freezing of liquid into a diamond structure might be severely hindered for a large range of pressures beyond the graphite/diamond/liquid triple point. In Ref. [47] it is also pointed out that at 6,000 K the equation of state shows a change of slope around the transition to the fourfold liquid. At even lower temperature this feature becomes more and more evident, but for temperatures lower than $\sim$4,500 K the liquid freezes into a mainly fourfold coordinated amorphous structure. This observation is consistent with quenching MD simulations [70, 73] to obtain the tetrahedral amorphous carbon. In those simulations a mainly threefold liquid freezes into an almost completely fourfold amorphous.

1.6 Summary and Outlook

We have demonstrated how a well designed semi-empirical potential (LCBOP) provides detailed insight in the properties of carbon at extreme conditions. Applying advanced molecular simulation techniques to the LCBOP model provides an accurate description of the melting of graphite and diamond and a detailed picture of the structure and thermodynamics of the liquid. A detailed analysis of the liquid structure over a wide range of pressures and temperature validates the most advance LCBOP model (LCBOPII) as competitive to state-of-the-art DFT models. Analysis of the liquid structure near the melting line reveals that the liquid undergoes

[8] A fourfold coordinated liquid with a rather pronounced diamond-like structure in the first coordination shell [47]).

profound structural changes, with the two- and threefold coordination dominant from the region near the graphite melting line and a range well into the region near the diamond melting line. This observation is expected to have strong implications on the process of homogeneous nucleation of liquid carbon into diamond as demonstrated in Refs. [30, 74], suggesting that the formation of diamond in Uranus and Neptune is kinetically suppressed.

The availability of a validated and accurate empirical potential such as the LCBOP family provides an optimal starting point for further exploration of properties of carbon materials. Of particular interest would be graphite and diamond nucleation, the (meta)stability of novel carbon phases such as carbyne or M-carbon, the structure, stability and nucleation of condensed nanostructures such as nanotube arrays, layered graphene materials. A detailed atomistic picture of these topics will contribute significantly to fundamental understanding in material and planetary science as well as providing important input for carbon-based technological applications

Acknowledgements We gratefully acknowledge F. Colonna, A. Fasolino, D. Frenkel, J. H. Los, and C. Valeriani for inspiring and useful discussions.

Appendix A. Chemical Potential as a Function of Density

Here, we show how to derive Eq. 1.9. One can always write:

$$\begin{aligned}\beta\mu(\rho) &= \beta\mu(\rho^{\Xi}) + \beta\Delta\mu \\ &= \beta\mu(\rho^{\Xi}) + \frac{\beta}{N}\left[F(\rho) - F(\rho^{\Xi}) + P(\rho)V - P(\rho^{\Xi})V^{\Xi}\right] \\ &= \beta\mu(\rho^{\Xi}) + \frac{\beta}{N}\left[\int_{\rho}^{\rho^{\Xi}} \frac{\partial F}{\partial \rho}\,\mathrm{d}\rho + \frac{P(\rho)}{\rho} - \frac{P(\rho^{\Xi})}{\rho^{\Xi}}\right] \end{aligned} \tag{1.10}$$

Working out the integral:

$$\int_{\rho}^{\rho^{\Xi}} \frac{\partial F}{\partial \rho}\,\mathrm{d}\rho = \int_{\rho}^{\rho^{\Xi}} \frac{PV}{\rho}\,\mathrm{d}\rho = N\int_{\rho}^{\rho^{\Xi}} \frac{P}{\rho^2}\,\mathrm{d}\rho \tag{1.11}$$

From the ansatz $P(\rho) = a + b\rho + c\rho^2$, one finds:

$$\int_{\rho}^{\rho^{\Xi}} \frac{a}{\rho^2} + \frac{b}{\rho} + c\,\mathrm{d}\rho = \left[-\frac{a}{\rho} + \frac{a}{\rho^{\Xi}} + b\ln\rho - b\ln\rho^{\Xi} + c(\rho - \rho^{\Xi})\right] \tag{1.12}$$

Putting this result into Eq. 1.10 and reordering the terms:

$$\begin{aligned}\beta\mu(\rho) &= \beta\mu(\rho^{\Xi}) - \frac{P(\rho^{\Xi})}{\rho^{\Xi}} \\ &\quad + \beta\left[-\frac{a}{\rho} + \frac{a}{\rho^{\Xi}} + b\ln\rho - b\ln\rho^{\Xi} + c(\rho - \rho^{\Xi}) + \frac{a}{\rho} + b + c\rho\right] \\ &= \frac{\beta F^{\Xi}}{N} + \beta\left[2c\rho + b(\ln\rho + 1) - c\rho^{\Xi} - b\ln\rho^{\Xi} + \frac{a}{\rho^{\Xi}}\right] \\ &= \frac{\beta F^{\Xi}}{N} + \beta\left[\frac{a}{\rho^{\Xi}} + b\ln\frac{\rho}{\rho^{\Xi}} + b + c\left(2\rho - \rho^{\Xi}\right)\right] \end{aligned} \tag{1.13}$$

References

1. Whittaker AG (1978) Science 200:4343
2. Smith PPK, Buseck PR (1982) Science 216:984
3. Li Q, Ma Y, Oganov AR, Wang H, Wang H, Xu Y, Cui T, Mao H-K, Zou G (2009) Phys Rev Lett 102:175506
4. Kroto HW, Heath JR, O'Brien SC, Curl RF, Smalley RE (1985) Nature 318:162
5. Iijima S (1991) Nature 354:56
6. Novoselov KS, Geim AK, Jiang SVMD, Zhang Y, Dubonos SV, Grigorieva IV, Firsov AA (2004) Science 306:666
7. Bundy FP (1963) J Chem Phys 38:631
8. Bundy FP (1963) J Chem Phys 38:618
9. Fateeva NS, Vereshchagin LF (1971) Pis'ma Zh Ekps Teor Fiz 13:157
10. Galli G, Martin RM, Car R, Parrinello M (1990) Science 250:1547
11. Shaner JW, Brown JM, Swenson AC, McQueen RG (1984) J Phys (Paris) Colloq 45:C8
12. Grumbach MP, Martin RM (1996) Phys Rev B 54:15730
13. Asinovskii EI, Kirillin AV, Kostanovskii AV (1997) High Temp 35:704
14. Asinovskii EI, Kirillin AV, Kostanovskii AV, Fortov VE (1998) High Temp 36:716
15. Bundy FP, Bassett WA, Weathers MS, Hemley RJ, Mao HK, Goncharov AF (1996) Carbon 34:141
16. Togaya M (1997) Phys Rev Lett 79:2474
17. Korsunskaya IA, Kamenetskaya DS, Aptekar IL (1972) Fiz Metal Metalloved 34:942 English version in: (1972) Phys. Met. Metallogr. (USSR) 34:39.
18. van Thiel M, Ree FH (1993) Phys Rev B 48:3591
19. Fried LE, Howard WM (2000) Phys Rev B 61:8734
20. Glosli JN, Ree FH (1999) Phys Rev Lett 82:4659
21. Glosli JN, Ree FH (1999) J Chem Phys 110:441
22. Wu CJ, Glosli JN, Galli G, Ree FH (2002) Phys Rev Lett 89:135701
23. Bradley DK, Eggert JH, Hicks DG, Celliers PM, Moon SJ, Cauble RC, Collins GW (2004) Phys Rev Lett 93:195506
24. Knudson MD, Desjarlais MP, Dolan DH (2008) Science 322:1822–1825
25. Yin MT, Cohen ML (1983) Phys Rev Lett 50:2006
26. Correa AA, Bonev SA, Galli G (2006) PNAS 103:1204–1208
27. Los JH, Fasolino A (2003) Phys Rev B 68:024107
28. Ghiringhelli LM, Los JH, Meijer EJ, Fasolino A, Frenkel D (2005) Phys Rev Lett 94:145701

29. Los JH, Ghiringhelli LM, Fasolino A, Meijer EJ (2005) Phys Rev B 72:214102. Erratum: Phys Rev B 73:229901 (2006)
30. Ghiringhelli LM, Valeriani C, Los JH, Meijer EJ, Fasolino A, Frenkel D (2008) Mol Phys 106:2011
31. Savvatimsky AI (2005) Carbon 43:1115
32. Bradley DK, Eggert JH, Smith RF, Prisbrey ST, Hicks DG, Braun DG, Biener J, Hamza AV, Rudd RE, Collinds GW (2009) Phys Rev Lett 102:075503
33. Brenner DW, Shenderova OA, Areshkin DA (1998) In: Lipkowitz KB, Boyd DB (eds.) Reviews in computational chemistry, vol 5. Wiley, New York
34. Tersoff J (1988) Phys Rev Lett 61:2879
35. Brenner DW (1990) Phys Rev B 42:9458. Erratum: Phys Rev B 46:1948 (1992)
36. Brenner DW, Harrison JH, White CT, Colton RJ (1991) Thin Solid Films 206:220
37. Brenner DW, Shenderova OA, Harrison JA, Stuart SJ, Ni B, Sinnott SB (2002) J Phys Condens Matter 14:783
38. Stuart SJ, Tutein AB, Harrison JA (2000) J Phys Chem 14:6472
39. Kum O, Ree FH, Stuart SJ, Wu CJ (2003) J Chem Phys 119:6053
40. Ghiringhelli LM (2006) On the nature of the phase transitions in covalent liquids. PhD thesis. It can be downloaded from: http://dare.uva.nl/document/18341/
41. Anwar J, Frenkel D, Noro MG (2003) J Chem Phys 118:728
42. Johnson JK, Zollweg JA, Gubbins KE (1993) Mol Phys 78:591
43. Frenkel D, Ladd JC (1984) J Chem Phys 81:3188
44. Frenkel D, Smit B (2002) Understanding molecular simulation. Academic Press, San Diego, CA
45. Polson JM, Trizac E, Pronk S, Frenkel D (2000) J Chem Phys 112:5339
46. Kofke DA (1993) J Chem Phys 98:4149
47. Ghiringhelli LM, Los JH, Meijer EJ, Fasolino A, Frenkel D (2004) Phys Rev B 69:100101(R)
48. Wang X, Scandolo S, Car R (2005) Phys Rev Lett 95:185701
49. Brygoo S, Henry E, Loubeyre P, Eggert J, Koenig M, Loupias B, Benuzzi-Meounaix A, Rabec le Gloahec M (2007) Nat Mater 6:274–277
50. Strässler S, Kittel C (1965) Phys Rev 139:A758
51. van Thiel M, Ree FH (1992) High Pressure Res 10:607
52. Tanaka H (2000) Phys Rev E 62:6968–6976
53. Ponyatovsky EG (2003) J Phys Condens Matter 15:6123
54. Morris JR, Wang CZ, Ho KM (1995) Phys Rev B 52:4138
55. Eppenga R, Frenkel D (1984) Mol Phys 52:1303
56. Vorholz J, Harismiadis VI, Panagiotopoulos AZ (1996) J Chem Phys 105:8469
57. Car R, Parrinello M (1985) Phys Rev Lett 55:2471
58. CPMD, version 3.3, developed by Hutter J, Alavi A, Deutsch T, Bernasconi M, Goedecker S, Marx D, Tuckerman M, Parrinello M, MPI für Festkörperforschung and IBM Zurich Research Laboratory (1995–1999)
59. Hoover WG (1985) Phys Rev A 31:1695
60. Becke AD (1988) Phys Rev A 38:3098
61. Perdew JP (1986) Phys Rev B 33:8822(R). Erratum Phys Rev B 34:7406 (1986)
62. Blöchl PE, Parrinello M (1992) Phys Rev B 45:9413
63. Harada A, Shimojo F, Hoshino K (2007) J Non-Crystal Solid 353:3519
64. Dacosta PG, Nielsen OH, Kunc K (1986) J Phys C Solid State Phys 19:3163
65. Ghiringhelli LM, Los JH, Fasolino A, Meijer EJ (2005) Phys Rev B 72:214103
66. Mishima O, Stanley HE (1998) Nature 396:329–335
67. Stanley HE, Buldyrev SV, Canpolat M, Mishima O, Sadr-Lahijany MR, Scala A, Starr FW (2000) Phys Chem Chem Phys 2:1551–1558
68. Franzese G, Malescio G, Skibinsky A, Buldyrev SV, Stanley HE (2001) Nature 409:692
69. Marks NA (2001) Phys Rev B 63:035401
70. Marks NA (2002) J Phys Condens Matter 14:2901
71. Galli G, Martin RM, Car R, Parrinello M (1989) Phys Rev Lett 63:988
72. Galli G, Martin RM, Car R, Parrinello M (1990) Phys Rev B 42:7470
73. Marks NA, Cooper NC, McKenzie DR, McCulloch DG, Bath P, Russo SP (2002) Phys Rev B 65:075411
74. Ghiringhelli LM, Valeriani C, Meijer EJ, Frenkel D (2007) Phys Rev Lett 99:055702